

# Probing Neutral Triple Gauge Couplings via $ZZ$ Production at $e^+e^-$ Colliders

John Ellis<sup>a</sup>, Hong-Jian He<sup>b,c</sup>, Rui-Qing Xiao<sup>d</sup>, Shi-Ping Zeng<sup>b</sup>

<sup>a</sup> Tsung-Dao Lee Institute, Shanghai Jiao Tong University, Shanghai, China;  
Department of Physics, King's College London, Strand, London WC2R 2LS, UK;  
Theoretical Physics Department, CERN, CH-1211 Geneva 23, Switzerland

<sup>b</sup> Tsung-Dao Lee Institute & School of Physics and Astronomy,  
Shanghai Jiao Tong University, Shanghai, China

<sup>c</sup> Department of Physics, Tsinghua University, Beijing, China;  
Center for High Energy Physics, Peking University, Beijing, China

<sup>d</sup> School of Physics, Peking University, Beijing, China

(john.ellis@cern.ch, hjhe@sjtu.edu.cn, xiaoruiqing@pku.edu.cn, spzeng@sjtu.edu.cn)

## Abstract

Neutral triple gauge couplings (nTGCs) first arise from the dimension-8 operators of the Standard Model Effective Field Theory (SMEFT), rather than the dimension-4 SM Lagrangian and dimension-6 SMEFT operators, opening up a unique window for probing new physics at the dimension-8 level. In this work, we formulate the nTGC form factors of  $ZZV^*$  ( $V = Z, \gamma$ ) that are compatible with the spontaneous breaking of the  $SU(2) \otimes U(1)$  electroweak gauge symmetry and consistently match the dimension-8 nTGC operators in the broken phase. We study the sensitivities for probing both the  $ZZV^*$  form factors and the corresponding new physics scales through  $ZZ$  production (with visible/invisible fermionic  $Z$  decays) at high energy  $e^+e^-$  colliders including CEPC, FCC-ee, ILC and CLIC. In particular, we identify the dimension-8 operator that contributes to the pure triple  $Z$  boson coupling  $ZZZ^*$  alone, but not the mixed  $ZZ\gamma^*$  coupling. We further study the correlations between probes of the  $ZZZ^*$  and  $ZZ\gamma^*$  couplings. We show that angular distributions of the final-state fermions can play key roles in suppressing the SM backgrounds and that the sensitivities can be improved by using polarized  $e^\mp$  beams. We demonstrate that machine learning is advantageous for handling the 4-body final states from  $ZZ$  decays and improves significantly the sensitivity reaches of probes of nTGCs in  $e^+e^-$  collisions. We find that nTGC new physics scales can be probed up to the multi-TeV scale at the proposed  $e^+e^-$  colliders.

KCL-PH-TH/2025-28, CERN-TH-2025-122

# Contents

<b>1 Introduction</b>	<b>2</b>
<b>2 <math>ZZV^*</math> Couplings from Operators and Form Factors</b>	<b>4</b>
2.1 nTGC Operators and Form Factors for $ZZV^*$ Couplings . . . . .	4
2.2 Unitarity Constraints on the CPC nTGCs . . . . .	7
<b>3 Scattering Amplitudes, Cross Sections and Angular Distributions</b>	<b>9</b>
<b>4 Probing <math>ZZV^*</math> Couplings at <math>e^+e^-</math> Colliders</b>	<b>17</b>
4.1 Analyzing $ZZ$ Production via Leptonic/Hadronic Channels . . . . .	18
4.2 Analyzing the Invisible Decay Channel $Z \rightarrow \nu\bar{\nu}$ . . . . .	19
4.3 Probability Cuts from Machine Learning . . . . .	21
4.4 Improvements from Polarized Electron and Positron Beams . . . . .	24
4.5 Analysis of Correlations between nTGC Parameters . . . . .	26
4.6 Comparison with Previous Results . . . . .	27
<b>5 Conclusions</b>	<b>29</b>
<b>References</b>	<b>30</b>

## 1 Introduction

Studies of neutral triple gauge couplings (nTGCs) open a unique window on new physics beyond the Standard Model (BSM), since they are absent both in the Standard Model (SM) and in the SM Effective Field Theory (SMEFT) [1] at the dimension-6 level. However, nTGCs are generated by dimension-8 SMEFT operators, and offer a rare opportunity to probe directly BSM physics at the dimension-8 level, without obscuration by dimension-4 SM contributions and dimension-6 SMEFT effects.

In a series of works [2]-[7], we have explored the potential sensitivities of probes of the nTGCs at  $e^+e^-$  and  $pp$  colliders through the reaction  $f\bar{f} \rightarrow Z\gamma$ , and further studied the UV completion of the nTGCs [8][9]. In the course of these studies, we have revisited the conventional nTGC form factor formalism [10][11], which respects only the residual  $U(1)_{\text{em}}$  gauge symmetry of QED. In our formulation of nTGC form factors we have emphasized [2]-[4] the importance of incorporating the full electroweak gauge group  $SU(2) \otimes U(1)$  of the SM with spontaneous symmetry breaking. In particular, we have shown that disregarding the full electroweak gauge group in the conventional nTGC formalism [10] gives unphysically large predictions for the nTGC sensitivity bounds that are stronger than the correct bounds by about two orders of magnitude in the cases of the LHC probes in initial CMS

and ATLAS experimental analyses [14][15]. However, the ATLAS collaboration [16] has recently performed a new LHC measurement of nTGCs by using the consistent nTGC form factor formulas [3][4] and confirmed our theoretical predictions for the prospective experimental sensitivities. The lesson is that, although the contributions of dimension-8 operators to collider processes generally have higher energy-power dependences than those of dimension-6 operators [12][13], it is important to ensure that high-energy behaviors of the dimension-8 contributions are consistent with the full electroweak gauge group  $SU(2)\otimes U(1)$  with spontaneous symmetry breaking, because it can impose nontrivial energy cancellations for the physical scattering amplitudes that arise from BRST identities [2]-[4].

Previous studies have mainly focused on analyses of  $Z\gamma$  production [2]-[7][17]. However, these cannot probe the pure  $Z$  boson nTGC  $ZZZ^*$ . For this purpose, we study in the present work a different reaction process,  $e^+e^- \rightarrow ZZ$  with on-shell final-state  $Z$  bosons, which can probe  $ZZZ^*$  and  $ZZ\gamma^*$  nTGCs. The final-state  $Z$  bosons decay dominantly through the charged-fermion channels and invisible channels<sup>1</sup>,  $Z \rightarrow q\bar{q}, \ell\bar{\ell}, \nu\bar{\nu}$ , whose angular distributions can be used to suppress the SM backgrounds and enhance the sensitivities of probes of the nTGCs. We demonstrate in our analysis how the sensitivities of probes of nTGCs can be enhanced by using polarized electron and positron ( $e^\mp$ ) beams and by using machine learning to optimize the discriminatory power of the 4-body final states from  $ZZ$  decays.<sup>2</sup>

This paper is organized as follows. In Section 2.1 we analyze how the nTGC couplings arise from dimension-8 SMEFT operators, and establish a consistent formulation of the nTGC form factors that incorporates the full electroweak gauge group  $SU(2)\otimes U(1)$  with spontaneous symmetry breaking. Then, in Section 2.2 we derive the unitarity constraints on nTGCs that are significantly weaker than the sensitivity reaches for probes of the nTGCs at high-energy  $e^+e^-$  colliders, as we show later. In Section 3 we derive the SM and nTGC contributions to the scattering amplitudes and cross sections for  $ZZ$  production channels, and analyze the differences between their angular distributions. Section 4 demonstrates how these may be used to probe  $ZZZ^*$  and  $ZZ\gamma^*$  nTGCs at high-energy  $e^+e^-$  colliders. We analyze the visible fermionic decay channels  $Z \rightarrow \ell\bar{\ell}, q\bar{q}$  in Section 4.1 and the invisible decay channels  $Z \rightarrow \nu\bar{\nu}$  in Section 4.2. We study the application of machine learning in Section 4.3 and analyze the improved sensitivities with polarized electron/positron beams in Section 4.4. A correlation analysis is presented in Section 4.5. Comparisons with previous analyses of probes of the nTGCs via the  $Z\gamma$  production channel are presented in Section 4.6. Finally, we conclude in Section 5.

<sup>1</sup>We note that at  $e^+e^-$  colliders, in contrast to  $pp$  colliders, it is possible to make a kinematic selection of invisible decays of on-shell  $Z$  bosons ( $Z \rightarrow \nu\bar{\nu}$ ) in the mixed final states  $ZZ \rightarrow \ell\bar{\ell}/q\bar{q} + \nu\bar{\nu}$ .

<sup>2</sup>In passing, we note that a recent preprint [18] studied  $ZZ$  production at  $e^+e^-$  colliders, but differs substantially from our work. It did not study the  $ZZZ^*$  coupling because it considered only the four operators  $\mathcal{O}_{\tilde{B}W}, \mathcal{O}_{B\tilde{W}}, \mathcal{O}_{\tilde{W}W}, \mathcal{O}_{\tilde{B}B}$  that do not contribute to the  $ZZZ^*$  vertex, as shown in our Table 1. Moreover, the operators  $\mathcal{O}_{\tilde{W}W}$  and  $\mathcal{O}_{\tilde{B}B}$  have zero contribution to the  $ZZ\gamma^*$  vertex as well, whereas  $\mathcal{O}_{B\tilde{W}}$  gives the same  $ZZ\gamma^*$  contribution as  $\mathcal{O}_{\tilde{B}W}$  (up to a trivial overall minus sign as shown in our Table 1). Hence, Ref. [18] effectively studied only the  $ZZ\gamma^*$  coupling generated by  $\mathcal{O}_{\tilde{B}W}$ , and could not study any correlations between different nTGCs as we do. Finally, it did not study the probe of any related nTGC form factors, which is a major subject of our work.

## 2 $ZZV^*$ Couplings from Operators and Form Factors

### 2.1 nTGC Operators and Form Factors for $ZZV^*$ Couplings

In previous papers [6][7] we studied possible probes of neutral triple gauge couplings (nTGCs) via on-shell  $Z\gamma$  production. In this Section, we will analyze the nTGC contributions to the production process  $e^-e^+ \rightarrow ZZ$  through the vertices  $ZZV^*$  (with  $V = Z, \gamma$ ). We work in the general framework of the Standard Model Effective Field Theory (SMEFT), in which nTGCs are first generated by dimension-8 operators [11]. The general dimension-8 SMEFT Lagrangian can be written as

$$\Delta\mathcal{L}(\text{dim-8}) = \sum_j \frac{c_j}{\tilde{\Lambda}^4} \mathcal{O}_j = \sum_j \frac{\text{sign}(c_j)}{\Lambda_j^4} \mathcal{O}_j = \sum_j \frac{1}{[\Lambda_j^4]} \mathcal{O}_j, \quad (2.1)$$

where the dimensionless coefficients  $c_j$  may be  $O(1)$ , with signs  $\text{sign}(c_j) = \pm$ . We define the corresponding cutoff scale  $\Lambda_j \equiv \tilde{\Lambda}/|c_j|^{1/4}$  and introduce the shorthand notation  $[\Lambda_j^4] \equiv \text{sign}(c_j)\Lambda_j^4$ .

A CP-conserving  $ZZV^*$  vertex can be parameterized as follows [11]:

$$ie\Gamma_{ZZV^*}^{\alpha\beta\mu}(q_1, q_2, q_3) = \frac{e(q_3^2 - M_V^2)}{M_Z^2} f_5^V \epsilon^{\mu\alpha\beta\rho} (q_1 - q_2)_\rho, \quad (2.2)$$

and a CP-conserving  $Z\gamma V^*$  vertex can be parameterized as follows [4]:

$$ie\Gamma_{Z\gamma V^*}^{\alpha\beta\mu}(q_1, q_2, q_3) = \frac{e(q_3^2 - M_V^2)}{M_Z^2} \left[ \left( h_3^V + \frac{h_4^V}{2M_Z^2} q_3^2 \right) q_{2\nu} \epsilon^{\alpha\beta\mu\nu} + \frac{h_4^V}{M_Z^2} q_2^\alpha q_{3\nu} q_{2\sigma} \epsilon^{\beta\mu\nu\sigma} \right]. \quad (2.3)$$

The  $ZZV^*$  nTGC vertices can arise only from dimension-8 operators with two SM Higgs-doublet fields. As shown in Ref. [8], we note that there are 7 independent CP-conserving nTGC operators of dimension-8 with two SM Higgs-doublet fields after taking into account the equivalence relations arising from integration by parts. We choose the following operator basis for our nTGC analysis:

$$\mathcal{O}_{\tilde{W}W} = iH^\dagger \tilde{W}_{\mu\nu} W^{\nu\rho} \{D_\rho, D_\mu\} H + \text{h.c.}, \quad (2.4a)$$

$$\mathcal{O}'_{\tilde{W}W} = iH^\dagger \tilde{W}_{\mu\nu} (D_\rho W^{\nu\rho}) D_\mu H + \text{h.c.}, \quad (2.4b)$$

$$\mathcal{O}_{\tilde{B}B} = iH^\dagger \tilde{B}_{\mu\nu} B^{\nu\rho} \{D_\rho, D_\mu\} H + \text{h.c.}, \quad (2.4c)$$

$$\mathcal{O}'_{\tilde{B}B} = iH^\dagger \tilde{B}_{\mu\nu} (D_\rho B^{\nu\rho}) D_\mu H + \text{h.c.}, \quad (2.4d)$$

$$\mathcal{O}_{\tilde{B}W} = iH^\dagger \tilde{B}_{\mu\nu} W^{\nu\rho} \{D_\rho, D_\mu\} H + \text{h.c.}, \quad (2.4e)$$

$$\mathcal{O}'_{\tilde{B}W} = iH^\dagger \tilde{B}_{\mu\nu} (D_\rho W^{\nu\rho}) D^\mu H + \text{h.c.}, \quad (2.4f)$$

$$\mathcal{O}_{\tilde{W}B} = iH^\dagger \tilde{W}_{\mu\nu} B^{\nu\rho} \{D_\rho, D_\mu\} H + \text{h.c.}, \quad (2.4g)$$

where  $H$  denotes the SM Higgs doublet and we define the dual field strengths  $\tilde{B}_{\mu\nu} = \epsilon_{\mu\nu\alpha\beta} B^{\alpha\beta}$  and  $\tilde{W}_{\mu\nu} = \epsilon_{\mu\nu\alpha\beta} W^{\alpha\beta}$ , where  $W_{\mu\nu} = W_{\mu\nu}^a \frac{\sigma^a}{2}$  and  $\sigma^a$  denotes the Pauli matrices. The above operators are all Hermitian and their Wilson coefficients  $c_j$  are assumed to be real, so that they conserve CP. The contributions of these operators to  $ZZZ^*$  and  $ZZ\gamma^*$  vertices are summarized in Table 1, where  $\langle H^0 \rangle = v/\sqrt{2}$  denotes the SM Higgs vacuum expectation value,  $\theta_W$  is the weak mixing angle, and we use the notations  $(s_W, c_W) = (\sin \theta_W, \cos \theta_W)$ .

We see that the operators  $\mathcal{O}_{\tilde{B}W}$  and  $\mathcal{O}_{\tilde{W}B}$  both contribute to the  $ZZ\gamma^*$  coupling, but do not contribute to the  $ZZZ^*$  coupling. Moreover, their contributions to the  $ZZ\gamma^*$  coupling differ only by an overall minus sign, so we need only consider the operator  $\mathcal{O}_{\tilde{B}W}$  for our study of the  $ZZ\gamma^*$  nTGC. In summary, we have 4 remaining relevant operators ( $\mathcal{O}'_{\tilde{W}W}, \mathcal{O}'_{\tilde{B}B}, \mathcal{O}_{\tilde{B}W}, \mathcal{O}'_{\tilde{B}W}$ ), among which  $\mathcal{O}_{\tilde{B}W}$  contributes to the  $ZZ\gamma^*$  coupling alone and the other three operators contribute to both the  $ZZZ^*$  and  $ZZ\gamma^*$  couplings.

We note in Table 1 that three dimension-8 operators ( $\mathcal{O}'_{\tilde{W}W}, \mathcal{O}'_{\tilde{B}B}, \mathcal{O}'_{\tilde{B}W}$ ) contribute to the  $ZZZ^*$  vertex, as follows:

$$f_5^Z = v^2 M_Z^2 \left( \frac{1}{4 \tan \theta_W [\Lambda'_{\tilde{W}W}]^4} + \frac{\tan \theta_W}{[\Lambda'_{\tilde{B}B}]^4} + \frac{1}{2 [\Lambda'_{\tilde{B}W}]^4} \right). \quad (2.5)$$

In order to study the  $ZZZ^*$  and  $ZZ\gamma^*$  couplings separately, we can construct an operator that contributes to the  $ZZZ^*$  coupling alone:

$$\mathcal{O}_{3Z} \equiv \mathcal{O}'_{\tilde{W}W} + \frac{1}{4} \mathcal{O}'_{\tilde{B}B}, \quad (2.6)$$

which yields the following  $ZZZ^*$  coupling:

$$\frac{ev^2}{4s_W c_W} (p_3^2 - M_Z^2) (p_1^\rho - p_2^\rho) \epsilon_{\alpha\beta\mu\rho}. \quad (2.7)$$

Its contribution to the  $ZZZ^*$  form factor  $f_5^Z$  is as follows:

$$f_5^Z = \frac{v^2 M_Z^2}{4s_W c_W [\Lambda_{3Z}^4]}. \quad (2.8)$$

We also see in Table 1 that there are four dimension-8 operators ( $\mathcal{O}'_{\tilde{W}W}, \mathcal{O}'_{\tilde{B}B}, \mathcal{O}_{\tilde{B}W}, \mathcal{O}'_{\tilde{B}W}$ ) that contribute to the  $ZZ\gamma^*$  vertex, whose contributions to the  $ZZ\gamma^*$  form factor are as follows:

$$f_5^\gamma = v^2 M_Z^2 \left( \frac{1}{4 [\Lambda'_{\tilde{W}W}]^4} + \frac{1}{[\Lambda'_{\tilde{B}B}]^4} + \frac{1}{2s_W c_W [\Lambda_{\tilde{B}W}]^4} + \frac{\tan \theta_W}{2 [\Lambda'_{\tilde{B}W}]^4} \right). \quad (2.9)$$

Operators/Couplings	$ZZZ^*$	$ZZ\gamma^*$
$\mathcal{O}_{\tilde{W}W}$	0	0
$\mathcal{O}'_{\tilde{W}W}$	$\frac{ev^2}{4 \tan \theta_W} (p_3^2 - M_Z^2) (p_1^\rho - p_2^\rho) \epsilon_{\alpha\beta\mu\rho}$	$\frac{ev^2}{4} p_3^2 (p_1^\rho - p_2^\rho) \epsilon_{\alpha\beta\mu\rho}$
$\mathcal{O}'_{\tilde{B}B}$	0	0
$\mathcal{O}'_{\tilde{B}B}$	$ev^2 \tan \theta_W (p_3^2 - M_Z^2) (p_1^\rho - p_2^\rho) \epsilon_{\alpha\beta\mu\rho}$	$-ev^2 p_3^2 (p_1^\rho - p_2^\rho) \epsilon_{\alpha\beta\mu\rho}$
$\mathcal{O}_{\tilde{B}W}$	0	$-\frac{ev^2}{2s_W c_W} p_3^2 (p_1^\rho - p_2^\rho) \epsilon_{\alpha\beta\mu\rho}$
$\mathcal{O}'_{\tilde{B}W}$	$\frac{ev^2}{2} (p_3^2 - M_Z^2) (p_1^\rho - p_2^\rho) \epsilon_{\alpha\beta\mu\rho}$	$\frac{ev^2}{2} \tan \theta_W p_3^2 (p_1^\rho - p_2^\rho) \epsilon_{\alpha\beta\mu\rho}$
$\mathcal{O}_{\tilde{W}B}$	0	$\frac{ev^2}{2s_W c_W} p_3^2 (p_1^\rho - p_2^\rho) \epsilon_{\alpha\beta\mu\rho}$

Table 1: Summary of contributions by the relevant CP-conserving dimension-8 operators to the nTGC vertices  $ZZZ^*$  and  $ZZ\gamma^*$ .

Among the above four operators, the operator  $\mathcal{O}_{\tilde{B}W}$  contributes to the form factor  $f_5^\gamma$  only, but not to  $f_5^Z$ . This is in contrast with the operator  $\mathcal{O}_{3Z}$ , which contributes to the form factor  $f_5^Z$  only, instead of  $f_5^\gamma$ . As discussed in Ref. [4], the operator  $\mathcal{O}_{\tilde{B}W}$  also contributes to the  $Z\gamma Z^*$  vertex, and the corresponding form factor  $h_3^Z$  is given as follows:

$$h_3^Z = \frac{v^2 M_Z^2}{2s_W c_W [\Lambda_{\tilde{B}W}^4]}. \quad (2.10)$$

Inspecting Eqs.(2.9) and (2.10), we deduce the following relation:

$$f_5^\gamma = h_3^Z, \quad (\text{for } \mathcal{O}_{\tilde{B}W}). \quad (2.11)$$

As seen in Eq.(2.4), spontaneous electroweak symmetry breaking (EWSB) and the Higgs vacuum expectation value (VEV) are essential for generating  $ZZV^*$  couplings. We also note that these vertices could only generate on-shell  $Z$  pairs with one  $Z$  polarized transversely and the other  $Z$  polarized longitudinally, since the kinematic structure with the antisymmetric Levi-Civita tensor causes the production of  $Z$  pairs with the same polarizations to vanish. Due to the antisymmetric structure, the pure gauge operators  $\mathcal{O}_{G\pm}$  that we introduced in Ref. [6] make vanishing contributions to the  $ZZV^*$  couplings.

Working in the electroweak broken phase of the SM in which  $SU(2)_W \otimes U(1)_Y \rightarrow U(1)_{\text{em}}$ , we expand the operators (2.4) and derive the relevant neutral triple gauge vertices (nTGVs) as follows:

$$\mathcal{O}_{\tilde{W}W} \rightarrow -\frac{ev^2}{8s_W c_W} \left( s_W^2 \tilde{A}_{\mu\nu} A^{\nu\rho} + s_W c_W \tilde{A}_{\mu\nu} Z^{\nu\rho} + s_W c_W \tilde{Z}_{\mu\nu} A^{\nu\rho} + c_W^2 \tilde{Z}_{\mu\nu} Z^{\nu\rho} \right) (\partial^\mu Z_\rho + \partial_\rho Z^\mu), \quad (2.12a)$$

$$\mathcal{O}'_{\tilde{W}W} \rightarrow -\frac{ev^2}{8s_W c_W} Z^\mu \left( s_W^2 \tilde{A}_{\mu\nu} \partial_\rho A^{\nu\rho} + s_W c_W \tilde{A}_{\mu\nu} \partial_\rho Z^{\nu\rho} + s_W c_W \tilde{Z}_{\mu\nu} \partial_\rho A^{\nu\rho} + c_W^2 \tilde{Z}_{\mu\nu} \partial_\rho Z^{\nu\rho} \right), \quad (2.12b)$$

$$\mathcal{O}_{\tilde{B}B} \rightarrow \frac{ev^2}{2s_W c_W} \left( -c_W^2 \tilde{A}_{\mu\nu} A^{\nu\rho} + s_W c_W \tilde{A}_{\mu\nu} Z^{\nu\rho} + s_W c_W \tilde{Z}_{\mu\nu} A^{\nu\rho} - s_W^2 \tilde{Z}_{\mu\nu} Z^{\nu\rho} \right) (\partial^\mu Z_\rho + \partial_\rho Z^\mu), \quad (2.12c)$$

$$\mathcal{O}'_{\tilde{B}B} \rightarrow -\frac{ev^2}{2s_W c_W} Z^\mu \left( c_W^2 \tilde{A}_{\mu\nu} \partial_\rho A^{\nu\rho} - s_W c_W \tilde{A}_{\mu\nu} \partial_\rho Z^{\nu\rho} - s_W c_W \tilde{Z}_{\mu\nu} \partial_\rho A^{\nu\rho} + s_W^2 \tilde{Z}_{\mu\nu} \partial_\rho Z^{\nu\rho} \right), \quad (2.12d)$$

$$\mathcal{O}_{\tilde{B}W} \rightarrow \frac{ev^2}{4s_W c_W} \left( s_W c_W \tilde{A}_{\mu\nu} A^{\nu\rho} + c_W^2 \tilde{A}_{\mu\nu} Z^{\nu\rho} - s_W^2 \tilde{Z}_{\mu\nu} A^{\nu\rho} - s_W c_W \tilde{Z}_{\mu\nu} Z^{\nu\rho} \right) (\partial^\mu Z_\rho + \partial_\rho Z^\mu), \quad (2.12e)$$

$$\mathcal{O}'_{\tilde{B}W} \rightarrow \frac{ev^2}{4s_W c_W} Z^\mu \left( s_W c_W \tilde{A}_{\mu\nu} \partial_\rho A^{\nu\rho} + c_W^2 \tilde{A}_{\mu\nu} \partial_\rho Z^{\nu\rho} - s_W^2 \tilde{Z}_{\mu\nu} \partial_\rho A^{\nu\rho} - s_W c_W \tilde{Z}_{\mu\nu} \partial_\rho Z^{\nu\rho} \right), \quad (2.12f)$$

$$\mathcal{O}_{\tilde{W}B} \rightarrow -\frac{ev^2}{4s_W c_W} \left( -s_W c_W \tilde{A}_{\mu\nu} A^{\nu\rho} + s_W^2 \tilde{A}_{\mu\nu} Z^{\nu\rho} - c_W^2 \tilde{Z}_{\mu\nu} A^{\nu\rho} + s_W c_W \tilde{Z}_{\mu\nu} Z^{\nu\rho} \right) (\partial^\mu Z_\rho + \partial_\rho Z^\mu). \quad (2.12g)$$

Combining the above contributions to the nTGC vertices, we can derive the general Lorenz structures for the  $ZZV^*$  vertices with the form factors ( $f_5^Z, f_5^\gamma$ ) in coordinate space that respect the residual gauge symmetry  $U(1)_{\text{em}}$  of QED:

$$\begin{aligned} \mathcal{L} = & \frac{e}{2M_Z^2} f_5^\gamma \left( c_W^2 \tilde{A}_{\mu\nu} Z^{\nu\rho} - s_W^2 \tilde{Z}_{\mu\nu} A^{\nu\rho} \right) (\partial^\mu Z_\rho + \partial_\rho Z^\mu) \\ & - \frac{e}{2M_Z^2} f_5^Z Z^\mu \tilde{Z}_{\mu\nu} \partial_\rho Z^{\nu\rho}. \end{aligned} \quad (2.13)$$

## 2.2 Unitarity Constraints on the CPC nTGCs

In this Section we analyze the perturbative unitarity constraints on the CPC nTGCs from the process  $e^-e^+ \rightarrow ZZ$ , finding that these constraints are much weaker than the sensitivity reaches of the collider analysis presented in the following Section.

We make a partial-wave expansion of the nTGC contributions to the scattering amplitude of  $e^-e^+ \rightarrow ZZ$  as follows [19]:

$$a_J = \frac{e^{i(\nu'-\nu)\phi}}{32\pi} \int_{-1}^1 d(\cos\theta) d_{\nu'\nu}^J(\cos\theta) \mathcal{T}_{\text{nTGC}}^{s_f s_{\bar{f}}, \lambda_{Z_1} \lambda_{Z_2}}, \quad (2.14)$$

where the differences between initial-state and final-state helicities are given by  $\nu = s_f - s_{\bar{f}}$  and  $\nu' = \lambda_{Z_1} - \lambda_{Z_2}$ , respectively. We note that it is sufficient to treat the initial-state electrons/positrons as massless, so we have  $s_f = -s_{\bar{f}}$ , leading to  $\nu = \pm 1$ . This implies that the  $J=1$  partial wave makes the leading contribution. The relevant Wigner  $d$  functions [20] are given by

$$d_{1,0}^1 = -\frac{1}{\sqrt{2}}, \quad d_{1,\pm 1}^1 = \frac{1}{2}(1 \pm \cos\theta), \quad (2.15)$$

and the relation  $d_{m,m'}^J = d_{-m,-m'}^J$  holds in general.

For the process  $e_L^- e_R^+ \rightarrow ZZ$ , we compute the leading contribution to the scattering amplitude  $\mathcal{T}_{\text{nTGC}}^{s_f s_{\bar{f}}, \lambda_{Z_1} \lambda_{Z_2}}$  as follows:

$$\mathcal{T}_{(8)}^{LR} = \pm \frac{c_L^V f_5^V e^2 s^{\frac{3}{2}}}{\sqrt{2} c_W s_W M_Z^3} \left( \sin^2 \frac{\theta}{2}, \cos^2 \frac{\theta}{2} \right), \quad (2.16)$$

and the corresponding leading  $p$ -wave amplitude  $a_1$  is given by

$$|\Re(a_1)| = \left| \frac{c_L^V f_5^V e^2 s^{\frac{3}{2}}}{48\sqrt{2} \pi c_W s_W M_Z^3} \right|. \quad (2.17)$$

The partial-wave unitarity condition is  $|\Re(a_1)| < 1$ , where we have included a factor of 2 as the final-state  $ZZ$  are identical particles [19]. Thus, we derive the following unitarity bound on the leading contributions to the nTGC form factor:

$$|f_5^V| < \left| \frac{48\sqrt{2} \pi c_W s_W M_Z^3}{c_L^V e^2 s^{\frac{3}{2}}} \right|. \quad (2.18)$$

Analogously, for the process  $e_R^- e_L^+ \rightarrow ZZ$ , we derive the following unitarity bound:

$$|f_5^V| < \left| \frac{48\sqrt{2} \pi c_W s_W M_Z^3}{c_R^V e^2 s^{\frac{3}{2}}} \right|, \quad (2.19)$$

which can be obtained from the unitarity bound (2.18) by the replacement  $c_L^V \leftrightarrow c_R^V$ . using these results we derive the following unitarity bounds on the nTGC form factors  $f_5^\gamma$  and  $f_5^Z$ :

$$|f_5^\gamma| < \frac{48\sqrt{2} \pi M_Z^3}{e^2 s^{\frac{3}{2}}}, \quad |f_5^Z| < \frac{96\sqrt{2} \pi c_W s_W M_Z^3}{e^2 (1-2s_W^2) s^{\frac{3}{2}}}. \quad (2.20)$$

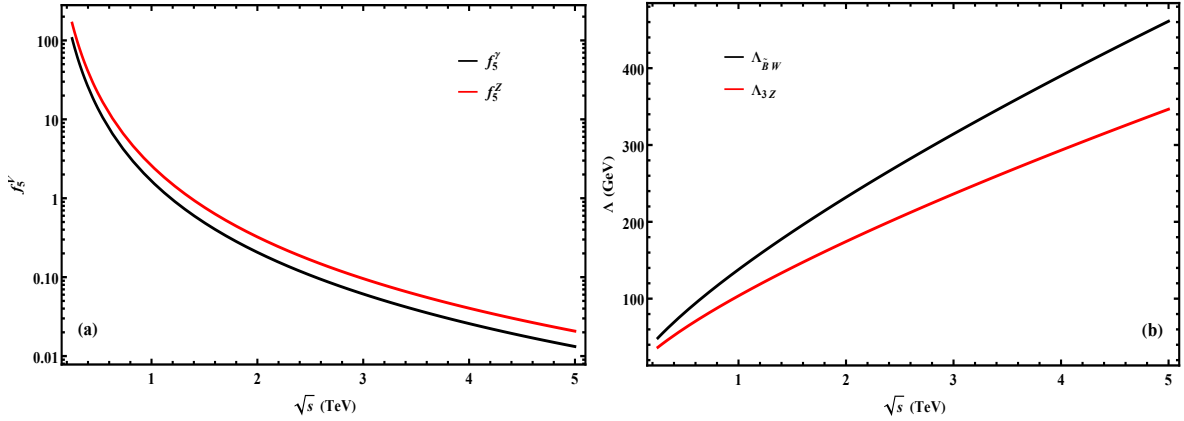


Figure 1: Unitarity bounds on the nTGC form factors  $f_5^\gamma$  and  $f_5^Z$  in plot (a) and on the new physics scales  $\Lambda_{\tilde{B}W}$  and  $\Lambda_{3Z}$  in plot (b). These bounds are derived from the  $p$ -wave amplitudes for the reaction  $e^-e^+ \rightarrow ZZ$ .

Since the nTGC form factors  $f_5^\gamma$  and  $f_5^Z$  are connected to the new physics cutoff scales  $\Lambda_{\tilde{B}W}$  and  $\Lambda_{3Z}$  of the corresponding dimension-8 nTGC operators as shown in Eqs.(2.9) and (2.8), we derive the following unitarity bounds on  $\Lambda_{\tilde{B}W}$  and  $\Lambda_{3Z}$ :

$$\Lambda_{\tilde{B}W} > \sqrt[4]{\frac{e^2 v^2 s^{3/2}}{96\sqrt{2}\pi s_W c_W M_Z}}, \quad \Lambda_{3Z} > \sqrt[4]{\frac{e^2 v^2 s^{3/2}(1-2s_W^2)}{384\sqrt{2}\pi s_W^2 c_W^2 M_Z}}. \quad (2.21)$$

$\sqrt{s}$ (TeV)	0.25	0.5	1	3	5
$\Lambda_{\tilde{B}W}$ (GeV)	48.8	82	138	314	461
$\Lambda_{3Z}$ (GeV)	36.6	61.6	104	236	347
$ f_5^\gamma $	106	13.2	1.65	0.061	0.013
$ f_5^Z $	166	20.7	2.59	0.096	0.021

Table 2: Unitarity bounds on the new physics scales  $\Lambda_{\tilde{B}W}$  and  $\Lambda_{3Z}$  (in GeV) of the dimension-8 nTGC operators and on the nTGC form factors  $f_5^\gamma$  and  $f_5^Z$ .

We present the unitarity bounds (2.20) and (2.21) for the reaction  $e^-e^+ \rightarrow ZZ$  in Table 2, for the representative  $e^+e^-$  collider energies  $\sqrt{s}=(0.25, 0.5, 1, 3, 5)$  TeV. We further present in Fig. 1 the unitarity bounds on the nTGC form factors and on the new physics scales of the nTGC operators as functions of the  $e^+e^-$  collision energy  $\sqrt{s}=(0.25, 0.5, 1, 3, 5)$  TeV for the reaction  $e^-e^+ \rightarrow ZZ$ . The unitarity bounds on the nTGC form factors  $f_5^\gamma$  and  $f_5^Z$  are shown in plot (a), and in plot (b) we display the unitarity bounds on the new physics scales  $\Lambda_{\tilde{B}W}$  and  $\Lambda_{3Z}$ . We find below that these unitarity bounds on the nTGC form factor ( $f_5^\gamma, f_5^Z$ ) and on the new physics scales ( $\Lambda_{\tilde{B}W}, \Lambda_{3Z}$ ) are much weaker than our collider constraints, and hence do not affect our collider analyses in the next Section.

### 3 Scattering Amplitudes, Cross Sections and Angular Distributions

In this Section we study the reaction  $e^-e^+ \rightarrow ZZ$  including contributions from both the SM and the nTGCs. For this purpose, we compute helicity amplitudes and cross sections, and analyze the angular distributions of its final states.

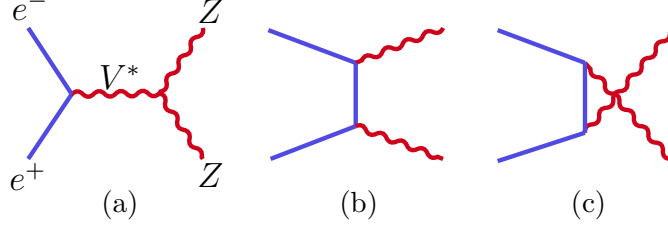


Figure 2: Feynman diagrams that contribute to the reaction  $e^-e^+ \rightarrow ZZ$ . Plot (a) shows the signal process containing the nTGC vertices  $ZZV^*$ , and plots (b) and (c) show the leading SM background contributions.

As shown in Fig. 2, the SM contributions to the reaction  $e^-e^+ \rightarrow ZZ$  are given by the  $t$ -channel and  $u$ -channel fermion-exchange diagrams, whereas the nTGC vertex  $ZZV^*$  contributes via  $s$ -channel diagrams mediated by a virtual  $Z$  or  $\gamma$ . We first derive the SM contributions to the scattering amplitudes of the reaction  $e^-(p_1)e^+(p_2) \rightarrow Z(p_3)Z(p_4)$ :

$$\mathcal{T}_{\text{sm}} = \bar{v}(p_2)\Gamma_Z^\mu \epsilon_\mu^*(p_4) \frac{(\not{p}_1 - \not{p}_3)}{t} \Gamma_Z^\nu \epsilon_\nu^*(p_3) u(p_1) + \bar{v}(p_2)\Gamma_Z^\mu \epsilon_\mu^*(p_3) \frac{(\not{p}_1 - \not{p}_4)}{u} \Gamma_Z^\nu \epsilon_\nu^*(p_4) u(p_1), \quad (3.1)$$

where we have defined the Mandelstam variables,  $s = (p_1 + p_2)^2$ ,  $t = (p_1 - p_3)^2$  and  $u = (p_1 - p_4)^2$ . In the above the vertex function  $\Gamma_Z^\mu$  is defined as follows:

$$\Gamma_Z^\mu = \frac{ie}{s_W c_W} \gamma^\mu (c_L^Z P_L + c_R^Z P_R), \quad (3.2)$$

where  $P_{L,R} = \frac{1 \mp \gamma_5}{2}$  are projection operators, and  $(c_L^Z, c_R^Z) = (-\frac{1}{2} + s_W^2, s_W^2)$  denote the (left, right)-handed gauge couplings of the electron to the  $Z$  boson, respectively.

Next we compute the new physics amplitudes contributed by the nTGCs for the reaction  $e^-(p_1)e^+(p_2) \rightarrow Z(p_3)Z(p_4)$ :

$$\begin{aligned} \mathcal{T}_{(8)} &= \bar{v}(p_2)\Gamma_V^\mu u(p_1) \frac{-g_{\mu\nu}}{s - M_V^2} ie \Gamma_{ZZV^*}^{\alpha\beta\nu} \epsilon_\alpha^*(p_3) \epsilon_\beta^*(p_4) \\ &= \bar{v}(p_2)\Gamma_V^\mu u(p_1) \frac{-eg_{\mu\nu}}{M_Z^2} f_5^V \epsilon^{\nu\alpha\beta\rho} (p_3 - p_4)_\rho \epsilon_\alpha^*(p_3) \epsilon_\beta^*(p_4), \end{aligned} \quad (3.3)$$

where we define the vertex functions  $\Gamma_V^\mu$  ( $V = \gamma, Z$ ) as follows:

$$\Gamma_V^\mu = \frac{ie}{s_W c_W} \gamma^\mu (c_L^V P_L + c_R^V P_R), \quad (3.4a)$$

$$c_L^\gamma = c_R^\gamma = -s_W c_W, \quad c_L^Z = -\frac{1}{2} + s_W^2, \quad c_R^Z = s_W^2, \quad (3.4b)$$

where  $c_L^V$  and  $c_R^V$  arise from the left-handed and right-handed gauge couplings of electrons to the

gauge bosons  $V = Z, \gamma$ , respectively.

For the reaction  $e^-(p_1) e^+(p_2) \rightarrow Z(p_3) Z(p_4)$ , we parameterize the external momenta as follows:

$$\begin{aligned} p_1 &= \frac{\sqrt{s}}{2}(1, 0, 0, 1), & p_2 &= \frac{\sqrt{s}}{2}(1, 0, 0, -1), \\ p_3 &= \left( \frac{\sqrt{s}}{2}, q \sin \theta, 0, q \cos \theta \right), & p_4 &= \left( \frac{\sqrt{s}}{2}, -q \sin \theta, 0, -q \cos \theta \right), \end{aligned} \quad (3.5)$$

where  $q = \sqrt{\frac{s}{4} - M_Z^2}$  is the magnitude of each  $Z$  boson's momentum.

In order to characterize the final state  $Z$  boson pair  $Z(p_3, \lambda) Z(p_4, \lambda')$  with its 9 helicity combinations, we define a  $3 \times 3$  matrix amplitude  $\mathcal{T}$  whose  $i$ -th row and  $j$ -th column element is defined as  $\mathcal{T}(i, j) \equiv \mathcal{T}(\lambda+2, \lambda'+2)$ . We derive the following SM contributions to the scattering amplitudes:

$$\begin{aligned} \mathcal{T}_{\text{sm}}^{\text{LR}} &= \frac{2e^2 c_L^2 Z^2}{s_W^2 c_W^2 (4M_Z^4 - 4\sin^2 \theta M_Z^2 s + s^2 \sin^2 \theta)} \times \\ &\left( \begin{array}{ccc} -sM_Z^2 \sin 2\theta & \sqrt{2s} M_Z (s \sin^2 \theta - 4M_Z^2 \sin^2 \frac{\theta}{2}) & -2s(s - 2M_Z^2) \sin \theta \sin^2 \frac{\theta}{2} \\ \sqrt{2s} M_Z (s \sin^2 \theta - 4M_Z^2 \cos^2 \frac{\theta}{2}) & 2sM_Z^2 \sin 2\theta & -\sqrt{2s} M_Z (s \sin^2 \theta - 4M_Z^2 \sin^2 \frac{\theta}{2}) \\ 2s(s - 2M_Z^2) \sin \theta \cos^2 \frac{\theta}{2} & -\sqrt{2s} M_Z (s \sin^2 \theta - 4M_Z^2 \cos^2 \frac{\theta}{2}) & -sM_Z^2 \sin 2\theta \end{array} \right), \end{aligned} \quad (3.6)$$

for the process  $e_L^- e_R^+ \rightarrow ZZ$ , and

$$\begin{aligned} \mathcal{T}_{\text{sm}}^{\text{RL}} &= \frac{2e^2 c_R^2 Z^2}{s_W^2 c_W^2 (4M_Z^4 - 4s \sin^2 \theta M_Z^2 + s^2 \sin^2 \theta)} \times \\ &\left( \begin{array}{ccc} -sM_Z^2 \sin 2\theta & \sqrt{2s} M_Z (s \sin^2 \theta - 4M_Z^2 \cos^2 \frac{\theta}{2}) & 2s(s - 2M_Z^2) \sin \theta \cos^2 \frac{\theta}{2} \\ \sqrt{2s} M_Z (s \sin^2 \theta - 4M_Z^2 \sin^2 \frac{\theta}{2}) & 2sM_Z^2 \sin 2\theta & -\sqrt{2s} M_Z (s \sin^2 \theta - 4M_Z^2 \cos^2 \frac{\theta}{2}) \\ -2s(s - 2M_Z^2) \sin \theta \sin^2 \frac{\theta}{2} & -\sqrt{2s} M_Z (s \sin^2 \theta - 4M_Z^2 \sin^2 \frac{\theta}{2}) & -sM_Z^2 \sin 2\theta \end{array} \right). \end{aligned} \quad (3.7)$$

for the process  $e_R^- e_L^+ \rightarrow ZZ$ .

As mentioned above, the  $ZZV^*$  coupling only contributes to the helicity amplitude for  $e^- e^+ \rightarrow ZZ$  with one longitudinally-polarized  $Z$  boson and one transversely-polarized  $Z$  boson:

$$\mathcal{T}_{(8)}^{\text{LR}} = \frac{c_L^V f_5^V e^2 \sqrt{s} (s - 4M_Z^2)}{\sqrt{2} c_W s_W M_Z^3} \begin{pmatrix} 0 & \sin^2 \frac{\theta}{2} & 0 \\ \cos^2 \frac{\theta}{2} & 0 & -\sin^2 \frac{\theta}{2} \\ 0 & -\cos^2 \frac{\theta}{2} & 0 \end{pmatrix}, \quad (3.8a)$$

$$\mathcal{T}_{(8)}^{\text{RL}} = \frac{c_R^V f_5^V e^2 \sqrt{s} (s - 4M_Z^2)}{\sqrt{2} c_W s_W M_Z^3} \begin{pmatrix} 0 & -\cos^2 \frac{\theta}{2} & 0 \\ -\sin^2 \frac{\theta}{2} & 0 & \cos^2 \frac{\theta}{2} \\ 0 & \sin^2 \frac{\theta}{2} & 0 \end{pmatrix}. \quad (3.8b)$$

Making a high-energy expansion, we deduce the high-energy behaviors of the helicity amplitudes from the contributions of the SM and the nTGCs, respectively:

$$\mathcal{T}_{\text{sm}} = \begin{pmatrix} O\left(\frac{M_Z^2}{E^2}\right) & O\left(\frac{M_Z}{E}\right) & O(E^0) \\ O\left(\frac{M_Z}{E}\right) & O\left(\frac{M_Z^2}{E^2}\right) & O\left(\frac{M_Z}{E}\right) \\ O(E^0) & O\left(\frac{M_Z}{E}\right) & O\left(\frac{M_Z^2}{E^2}\right) \end{pmatrix}, \quad (3.9a)$$

$$\mathcal{T}_{(8)} = \begin{pmatrix} 0 & O\left(\frac{E^3}{M_Z^3 \Lambda^4}\right) & 0 \\ O\left(\frac{E^3}{M_Z^3 \Lambda^4}\right) & 0 & O\left(\frac{E^3}{M_Z^3 \Lambda^4}\right) \\ 0 & O\left(\frac{E^3}{M_Z^3 \Lambda^4}\right) & 0 \end{pmatrix}, \quad (3.9b)$$

where we denote the energy scale  $E = \sqrt{s}$ . We see from Eq.(3.9a) that the SM amplitude with the final states  $Z_L Z_T$  would behave like  $\mathcal{T}_{\text{sm}}(Z_L Z_T) = O\left(\frac{M_Z}{\sqrt{s}}\right)$  at high energies.

This behavior can be understood via the electroweak equivalence theorem (ET) that connects the scattering amplitude of longitudinal gauge bosons to the scattering amplitude of the corresponding Goldstone bosons [21]. For the current scattering process we have the following ET relation:

$$\mathcal{T}[Z_L, Z_T] = \mathcal{T}[-i\pi^0, Z_T] + B[v, Z_T], \quad (3.10)$$

where  $\pi^0$  denotes the neutral Goldstone boson that is converted to the longitudinal mode  $Z_L$  via the Higgs mechanism [22]. In Eq.(3.10), the  $B$  term is defined as  $B = \mathcal{T}[v, Z_T]$ , with  $v \equiv v_\mu Z^\mu$  and  $v^\mu = \epsilon_L^\mu - \epsilon_S^\mu = O(M_Z/E)$ . Since the initial-state fermion masses are negligible, the SM contributions contain only the  $t$ - and  $u$ -channel exchanges. Thus we can deduce

$$\mathcal{T}_{\text{sm}}[\pi^0, Z_T] \simeq 0, \quad \mathcal{T}_{\text{sm}}[Z_L, Z_T] \simeq B = O\left(\frac{M_Z}{\sqrt{s}}\right), \quad (3.11)$$

which explains the high-energy behavior of  $\mathcal{T}_{\text{sm}}[Z_L Z_T]$ . Moreover, Eq.(3.9a) shows that  $\mathcal{T}_{\text{sm}}[Z_L Z_L] = O(M_Z^2/E^2)$ . This is because the ET gives

$$\mathcal{T}[Z_L, Z_L] = -\mathcal{T}[\pi^0, \pi^0] + B[LL], \quad (3.12)$$

where  $\mathcal{T}[\pi^0, \pi^0] = 0$  holds because the initial-state fermions  $e^\mp$  have very small masses, so that the Yukawa couplings between the Higgs boson (Goldstone boson) and fermions can be ignored. Hence, for the ET identity (3.12), we deduce the following:

$$\mathcal{T}[Z_L, Z_L] = B[LL] = \mathcal{T}[-i\pi^0, v] + \mathcal{T}[v, -i\pi^0] + \mathcal{T}[v, v] = \mathcal{T}[v, v] = O\left(\frac{M_Z^2}{E^2}\right). \quad (3.13)$$

We can then compute the SM contributions to amplitude-squared as follows:

$$\begin{aligned} \overline{|\mathcal{T}_{\text{sm}}|^2}[ZZ] &= \frac{e^4 s (c_L^{Z^4} + c_R^{Z^4}) [16M_Z^6 (1 + \cos^2\theta) - 4(3 - 7\cos^2\theta + 4s\cos^4\theta)M_Z^4]}{c_W^4 s_W^4 (4M_Z^4 - 4s\sin^2\theta M_Z^2 + s^2\sin^2\theta)^2} \\ &\quad - \frac{e^4 s (c_L^{Z^4} + c_R^{Z^4}) [8s^2\sin^2\theta\cos^2\theta M_Z^2 + s^3(\cos^4\theta - 1)]}{c_W^4 s_W^4 (4M_Z^4 - 4s\sin^2\theta M_Z^2 + s^2\sin^2\theta)^2}, \end{aligned} \quad (3.14)$$

where we average over the spins of the initial-state fermions and sum over the helicity combinations of the final states. The squared scattering amplitudes for the SM contributions to the final states  $Z_L Z_T$  and  $Z_T Z_L$  take the following form:

$$\overline{|\mathcal{T}_{\text{sm}}|^2}[Z_L Z_T] = \frac{2e^4 s M_Z^2 (c_L^{Z^4} + c_R^{Z^4}) [4(1 + \cos^2\theta)M_Z^4 - 4s\sin^2\theta M_Z^2 + s^2\sin^4\theta]}{c_W^4 s_W^4 (4M_Z^4 - 4s\sin^2\theta M_Z^2 + s^2\sin^2\theta)^2}. \quad (3.15)$$

We have verified that our above formulae (3.14) and (3.15) agree with the literature [11]. We can

further derive the SM contributions to the squared amplitudes for the final states  $Z_L Z_L$  and  $Z_T Z_T$ :

$$\overline{|\mathcal{T}_{\text{sm}}|^2}[Z_L Z_L] = \frac{e^4 s^2 M_Z^4 (c_L^{Z^4} + c_R^{Z^4}) \sin^2 2\theta}{c_W^4 s_W^4 (4M_Z^4 - 4s \sin^2 \theta M_Z^2 + s^2 \sin^2 \theta)^2}, \quad (3.16a)$$

$$\overline{|\mathcal{T}_{\text{sm}}|^2}[Z_T Z_T] = \frac{e^4 s^2 (c_L^{Z^4} + c_R^{Z^4}) [4(1 + 2 \cos^2 \theta) M_Z^4 - 4s(1 + \cos^2 \theta) M_Z^2 + s^2(1 + \cos^2 \theta)] \sin^2 \theta}{8c_W^4 s_W^4 (4M_Z^4 - 4s \sin^2 \theta M_Z^2 + s^2 \sin^2 \theta)^2}. \quad (3.16b)$$

As we have discussed earlier, the new physics of  $ZZV^*$  nTGCs contribute only to the reaction  $e^-(p_1)e^+(p_2) \rightarrow Z(p_3)Z(p_4)$  with the final states  $Z_L Z_T$  and  $Z_T Z_L$ . Computing the interference between the contributions from the dimension-8 nTGC operator and from the SM, we find the following form:

$$2\Re(\overline{\mathcal{T}_{\text{sm}} \mathcal{T}_{(8)}^*})[Z_L Z_T] = \frac{2s e^4 f_5^V (c_L^V c_L^{Z^2} - c_R^V c_R^{Z^2}) (4M_Z^2 - s) [2M_Z^2 (1 + \cos^2 \theta) - s \sin^2 \theta]}{c_W^3 s_W^3 M_Z^2 (4M_Z^4 - 4s \sin^2 \theta M_Z^2 + s^2 \sin^2 \theta)}. \quad (3.17)$$

This interference term is of  $O(\Lambda^{-4})$ . We can further compute the squared amplitude of  $O(\Lambda^{-8})$  from the dimension-8 nTGC contributions as follows:

$$\overline{|\mathcal{T}_{(8)}|^2}[Z_L Z_T] = \frac{e^4 s f_5^{V^2} (c_L^{V^2} + c_R^{V^2}) (s - 4M_Z^2)^2 (3 + \cos 2\theta)}{4s_W^2 c_W^2 M_Z^6}. \quad (3.18)$$

According to the energy power counting results (3.9), we can infer the leading high-energy behavior of each contribution to the squared amplitude  $|\mathcal{T}|^2$ :

$$|\mathcal{T}_{\text{sm}}|^2 \sim E^0, \quad \sum_{\lambda, \lambda'} \mathcal{T}_{\text{sm}}(\lambda \lambda') \mathcal{T}_{(8)}^*(\lambda \lambda') \sim E^2, \quad |\mathcal{T}_{(8)}|^2 \sim E^6. \quad (3.19)$$

However, we recall that the  $Z$  boson is unstable and decays inside the detector. The intermediate-state  $Z$  bosons with different polarizations interfere, and the leading high-energy dependence of  $\mathcal{T}_{\text{sm}} \mathcal{T}_{(8)}^*$  is  $E^3$ .

Using these results, we derive the total cross section of the reaction  $e^- e^+ \rightarrow ZZ$  as follows:

$$\begin{aligned} \sigma = & \frac{e^4 (c_L^{Z^4} + c_R^{Z^4}) \left[ -2s\beta(s - 2M_Z^2) + (4M_Z^4 + s^2) \ln \frac{s(1+\beta) - 2M_Z^2}{s(1-\beta) - 2M_Z^2} \right]}{16\pi c_W^4 s_W^4 (s - 2M_Z^2) s^2} \\ & + \frac{e^4 f_5^V (c_L^V c_L^{Z^2} - c_R^V c_R^{Z^2}) \left[ s(s + 2M_Z^2)\beta + 4M_Z^2 (s - M_Z^2) \operatorname{arccoth} \left( \frac{2M_Z^2 - s}{\beta s} \right) \right]}{16\pi c_W^3 s_W^3 M_Z^2 s^2} \\ & + \frac{e^4 f_5^{V^2} (c_L^{V^2} + c_R^{V^2}) \beta^5 s^2}{192\pi c_W^2 s_W^2 M_Z^6}, \end{aligned} \quad (3.20)$$

where  $\beta = p_Z/E_Z = \sqrt{1 - 4M_Z^2/s}$  and the symbol ‘‘arccoth’’ denotes the inverse function of the hyperbolic tangent function coth. In the high-energy limit, we can deduce the following behaviors for each contribution to the total cross section:

$$\sigma = O(s^{-1}) + O\left(\frac{s^0 M_Z^2}{\Lambda^4}\right) + O\left(\frac{s^2 M_Z^2}{\Lambda^8}\right). \quad (3.21)$$

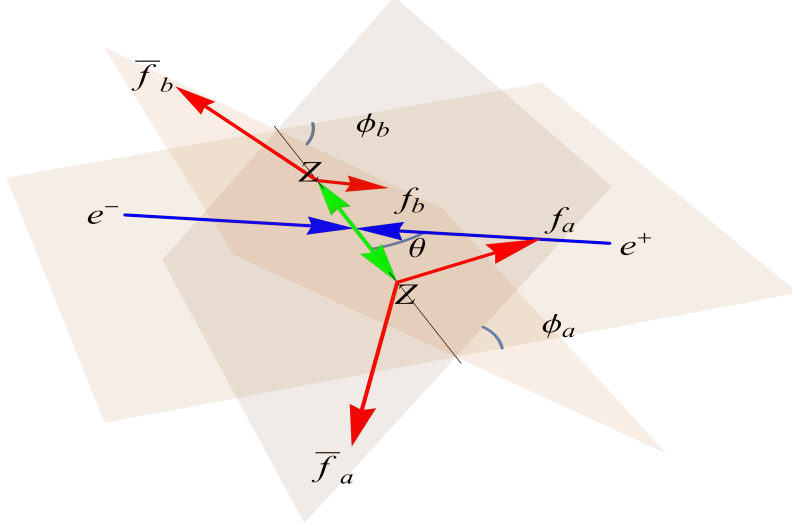


Figure 3: Kinematic structure of the reaction  $e^-e^+ \rightarrow ZZ$  followed by the fermionic decays  $Z \rightarrow f\bar{f}$ , in the  $e^-e^+$  collision frame.

We see that the SM contribution scales as  $s^{-1}$  and decreases with energy, whereas the interference term scales as  $s^0/\Lambda^4$  and thus is insensitive to the energy. Finally, the last contribution (arising from the squared amplitude) scales as  $s^2/\Lambda^8$  and increases with energy rapidly.

For the current analysis, we define the following normalized angular distribution functions:

$$f_\theta^j = \frac{1}{\sigma_j} \frac{d\sigma_j}{d\theta}, \quad (3.22)$$

where  $\sigma_j$  (with  $j=0, 1, 2$ ) represents the SM contribution ( $\sigma_0$ ), the  $O(\Lambda^{-4})$  contribution is ( $\sigma_1$ ), and the  $O(\Lambda^{-8})$  contribution is ( $\sigma_2$ ). Then, we compute the angular distribution functions as follows:

$$f_\theta^0 = \frac{s^2\beta(2M_Z^2-s)\left\{192M_Z^6-32sM_Z^4-8s^2M_Z^2+5s^3-s\beta^2[4\cos 2\theta(s+2M_Z^2)^2+s^2\beta^2\cos 4\theta]\right\}\sin\theta}{16\left[2s\beta(s-2M_Z^2)+(s^2+4M_Z^4)\ln\frac{s(1-\beta)-2M_Z^2}{s(1+\beta)-2M_Z^2}\right](4M_Z^4+s^2\beta^2\sin^2\theta)^2}, \quad (3.23a)$$

$$f_\theta^1 = -\frac{s^3\beta^3[6M_Z^2-s+(s+2M_Z^2)\cos 2\theta]\sin\theta}{4\left[s\beta(s+2M_Z^2)+4M_Z^2(s-M_Z^2)\operatorname{arccoth}\frac{2M_Z^2-s}{\beta s}\right](4M_Z^4+s^2\beta^2\sin^2\theta)}, \quad (3.23b)$$

$$f_\theta^2 = \frac{3}{16}(3+\cos 2\theta)\sin\theta. \quad (3.23c)$$

We see in Fig. 4 that the SM distribution is concentrated around the forward and backward scattering regions with  $\theta$  close to  $0^\circ$  or  $180^\circ$ . This feature is particularly clear for large collision energies  $\sqrt{s} \gg M_Z$ . It also shows that the interference distributions of  $O(\Lambda^{-4})$  have negative sign in the small  $\sin\theta$  region, namely, when the scattering angle  $\theta$  obeys the condition  $|\sin\theta| < 2M_Z/(s+2M_Z^2)^{1/2}$ .

Next, we further incorporate the fermionic decays of the final states  $ZZ$ . We first consider  $Z$  decay in its rest frame,  $Z(q_1) \rightarrow f(k_1)\bar{f}(k_2)$ , and express the momenta of the final-state fermions as follows:

$$k_1 = k(1, \sin\theta_a \cos\phi_a, \sin\theta_a \sin\phi_a, \cos\theta_a), \quad (3.24a)$$

$$k_2 = k(1, -\sin\theta_a \cos\phi_a, -\sin\theta_a \sin\phi_a, -\cos\theta_a), \quad (3.24b)$$

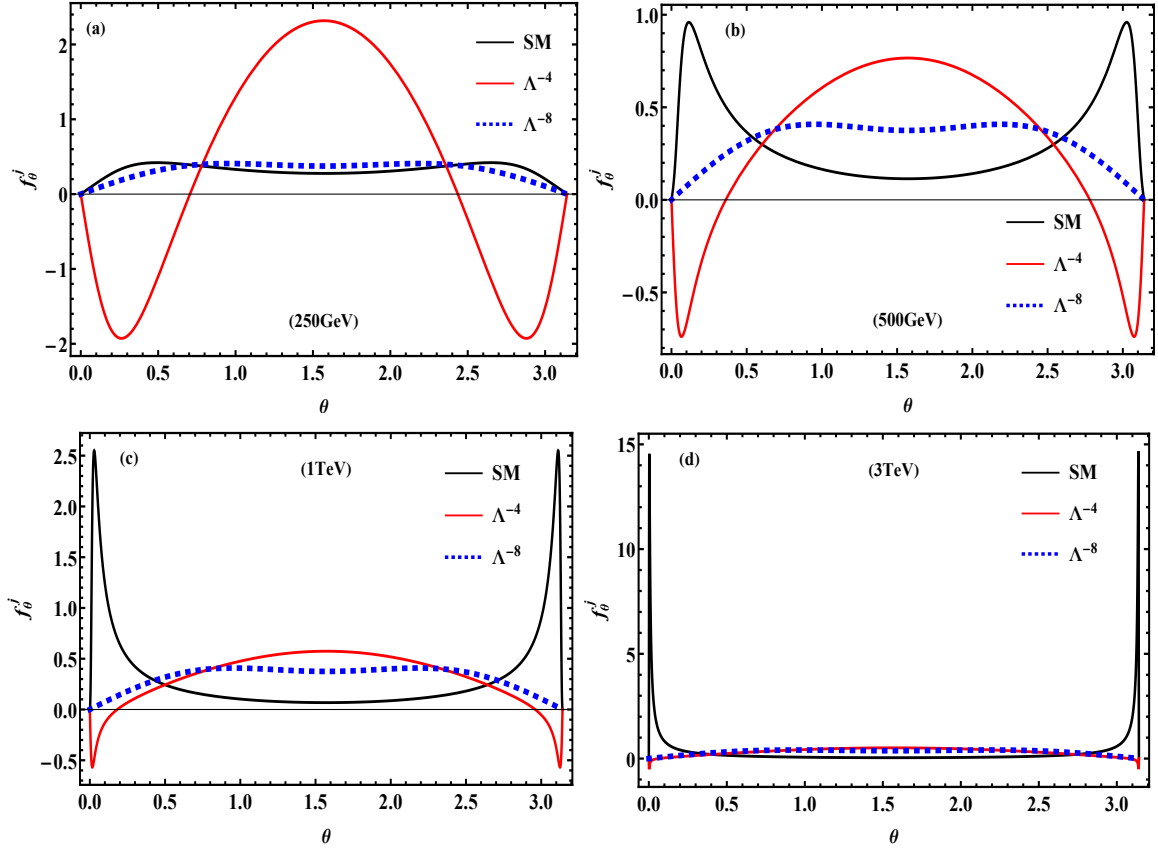


Figure 4: Normalized angular distributions in the polar scattering angle  $\theta$  for different collider energies,  $\sqrt{s} = (0.25, 0.5, 1, 3)$  TeV, are shown in plots (a)-(d) respectively. In each plot, the black, red and blue curves denote the contributions from the SM, the  $O(\Lambda^{-4})$  term, and the  $O(\Lambda^{-8})$  term, respectively.

where  $k = \frac{1}{2}M_Z$  holds since we treat the final-state fermions as effectively massless. Here the positive direction  $\hat{z}_a$  in the  $Z$  rest frame is chosen to be the  $Z$  moving direction in the laboratory frame, and  $\theta_a$  denotes the angle between the positive direction  $\hat{z}_a$  and the fermion  $f$  direction of motion in the  $Z$  rest frame. We define  $\phi_a$  as the angle between the  $e^-e^+$  scattering plane and the  $Z$ -decay plane in the  $e^-e^+$  center-of-mass frame. Similarly, we can express the kinematics of the other  $Z$  decay in terms of the angular variables  $\theta_b$  and  $\phi_b$ .

Then, we express the helicity amplitude for the reaction  $e^-e^+ \rightarrow ZZ \rightarrow f_a \bar{f}_a f_b \bar{f}_b$  as follows:

$$\begin{aligned}
\mathcal{T} = & \frac{e^2 M_Z^2 \mathcal{D}_Z(q_1) \mathcal{D}_Z(q_2)}{2s_W^2 c_W^2} \sum_{\lambda, \lambda' = -1}^1 e^{-i(\lambda\phi_a + \lambda'\phi_b)} \mathcal{T}_{ss'}[\lambda\lambda'] \\
& \times \left\{ (1 - \delta_\lambda^0) [f_R^a (1 - \lambda \cos\theta_a) - f_L^a (1 + \lambda \cos\theta_a)] + \sqrt{2} \delta_\lambda^0 \sin\theta_a (f_R^a + f_L^a) \right\} \\
& \times \left\{ (1 - \delta_{\lambda'}^0) [f_R^b (1 - \lambda' \cos\theta_b) - f_L^b (1 + \lambda' \cos\theta_b)] + \sqrt{2} \delta_{\lambda'}^0 \sin\theta_b (f_R^b + f_L^b) \right\}, \quad (3.25)
\end{aligned}$$

where  $D_Z$  is the propagator of the  $Z$  boson, and  $(f_L^{a,b}, f_R^{a,b}) = (f_L \delta_{\sigma, -\frac{1}{2}}, f_R \delta_{\sigma, \frac{1}{2}})$  denote the gauge couplings of the fermions  $a$  and  $b$  with helicity  $\sigma$ . In the above, the gauge couplings  $(f_L, f_R) = (T_3 - Qs_W^2, -Qs_W^2)$  denote the gauge couplings of the (left, right)-handed fermions. In Eq.(3.25),

$\mathcal{T}_{ss'}[\lambda\lambda']$  represents the on-shell helicity amplitude of the scattering process  $e^-e^+ \rightarrow ZZ$ :

$$\mathcal{T}_{ss'}[\lambda\lambda'] = \mathcal{T}_{\text{sm}}^{ss'}[\lambda\lambda'] + \mathcal{T}_{(8)}^{ss'}[\lambda\lambda'], \quad (3.26)$$

which include the contributions from both the SM and the dimension-8 nTGC operators.

Next, we derive the following normalized angular distributions  $f_{\theta_a}^j = \frac{1}{\sigma_j} \frac{d\sigma_j}{d\theta_a}$  as functions of the angle  $\theta_a$ :

$$f_{\theta_a}^0 = \frac{3 \sin \theta_a (s - 2M_Z^2) [3s - 10M_Z^2 + (s + 2M_Z^2) \cos 2\theta_a]}{16\beta \left[ s(s - 2M_Z^2)\beta + (s^2 + 4M_Z^4) \operatorname{arccoth} \frac{2M_Z^2 - s}{\beta s} \right]} + \frac{6 \sin \theta_a [(1 + \cos^2 \theta_a)(s^3 - 4s^2 M_Z^2 + 4s M_Z^4 + 8M_Z^6) - 32M_Z^6] \operatorname{arccoth} \frac{2M_Z^2 - s}{\beta s}}{16\beta^2 s \left[ s(s - 2M_Z^2)\beta + (s^2 + 4M_Z^4) \operatorname{arccoth} \frac{2M_Z^2 - s}{\beta s} \right]}, \quad (3.27a)$$

$$f_{\theta_a}^1 = f_{\theta_a}^2 = \frac{3}{32} \sin \theta_a (5 - \cos 2\theta_a), \quad (3.27b)$$

and the following normalized angular distributions  $f_{\phi_a}^j = \frac{1}{\sigma_j} \frac{d\sigma_j}{d\phi_a}$  with respect to the angle  $\phi_a$ :

$$f_{\phi_a}^0 = \frac{1}{2\pi} + \frac{3\pi\sqrt{s}\beta M_Z^3 f_-^2 (c_L^{Z^4} - c_R^{Z^4}) \cos \phi_a}{8f_+^2 (c_L^{Z^4} + c_R^{Z^4}) \left[ s(s - 2M_Z^2)\beta + (s^2 + 4M_Z^4) \operatorname{arccoth} \frac{2M_Z^2 - s}{\beta s} \right]} - \frac{M_Z^2 (s - 2M_Z^2) \left[ s\beta + (s - 2M_Z^2) \operatorname{arccoth} \frac{2M_Z^2 - s}{\beta s} \right] \cos 2\phi_a}{2\pi\beta^2 s \left[ s(s - 2M_Z^2)\beta + (s^2 + 4M_Z^4) \operatorname{arccoth} \frac{2M_Z^2 - s}{\beta s} \right]}, \quad (3.28a)$$

$$f_{\phi_a}^1 = \frac{1}{2\pi} - \frac{3\pi\beta^3 f_-^2 s^{\frac{3}{2}} (3s - 8M_Z^2) (c_L^V c_L^{Z^2} + c_R^V c_R^{Z^2}) \cos \phi_a}{256M_Z f_+^2 (c_L^V c_L^{Z^2} - c_R^V c_R^{Z^2}) \left[ s(s + 2M_Z^2)\beta + 4M_Z^2 (s - M_Z^2) \operatorname{arccoth} \frac{2M_Z^2 - s}{\beta s} \right]} - \frac{\left[ s(s - 2M_Z^2)\beta + 4M_Z^4 \operatorname{arccoth} \frac{2M_Z^2 - s}{\beta s} \right] \cos 2\phi_a}{8\pi \left[ s(s + 2M_Z^2)\beta + 4M_Z^2 (s - M_Z^2) \operatorname{arccoth} \frac{2M_Z^2 - s}{\beta s} \right]}, \quad (3.28b)$$

$$f_{\phi_a}^2 = \frac{1}{2\pi} - \frac{\cos 2\phi_a}{16\pi}, \quad (3.28c)$$

where we have defined the notations  $f_{\pm}^2 = f_L^2 \pm f_R^2$ , with  $(f_L, f_R) = (T_3 - Qs_W^2, -Qs_W^2)$  denoting gauge couplings of the (left, right)-handed fermions in the final states. The other notations  $(c_L^V, c_R^V)$  denote the gauge couplings of the (left, right)-handed  $e^{\mp}$  with the SM gauge boson  $V (= Z, \gamma)$  as defined in Eq.(3.4b).

Using the above analytical formulas, we present numerical results for the normalized angular distribution functions of  $\theta$ ,  $\theta_a$ , and  $\phi_a$  in Figs. 4, 5, and 6, respectively. In each figure, the four plots have input different collision energies,  $\sqrt{s} = (0.25, 0.5, 1, 3)$  TeV, corresponding to the expected collision energies of the CEPC, FCC-ee, ILC and its possible energy upgrades, and the design energy of CLIC. In Figs. 4 and 5 we use black, red and blue curves to denote the contributions from the SM, the  $O(\Lambda^{-4})$  interference, and the  $O(\Lambda^{-8})$  term, respectively. In Fig. 6, we use black, red, green and blue curves to denote the contributions from the SM, the  $O(\Lambda^{-4})$  interference with  $\gamma^*$ , the  $O(\Lambda^{-4})$  interference with  $Z^*$ , and the  $O(\Lambda^{-8})$  term, respectively. We find that the distributions with respect

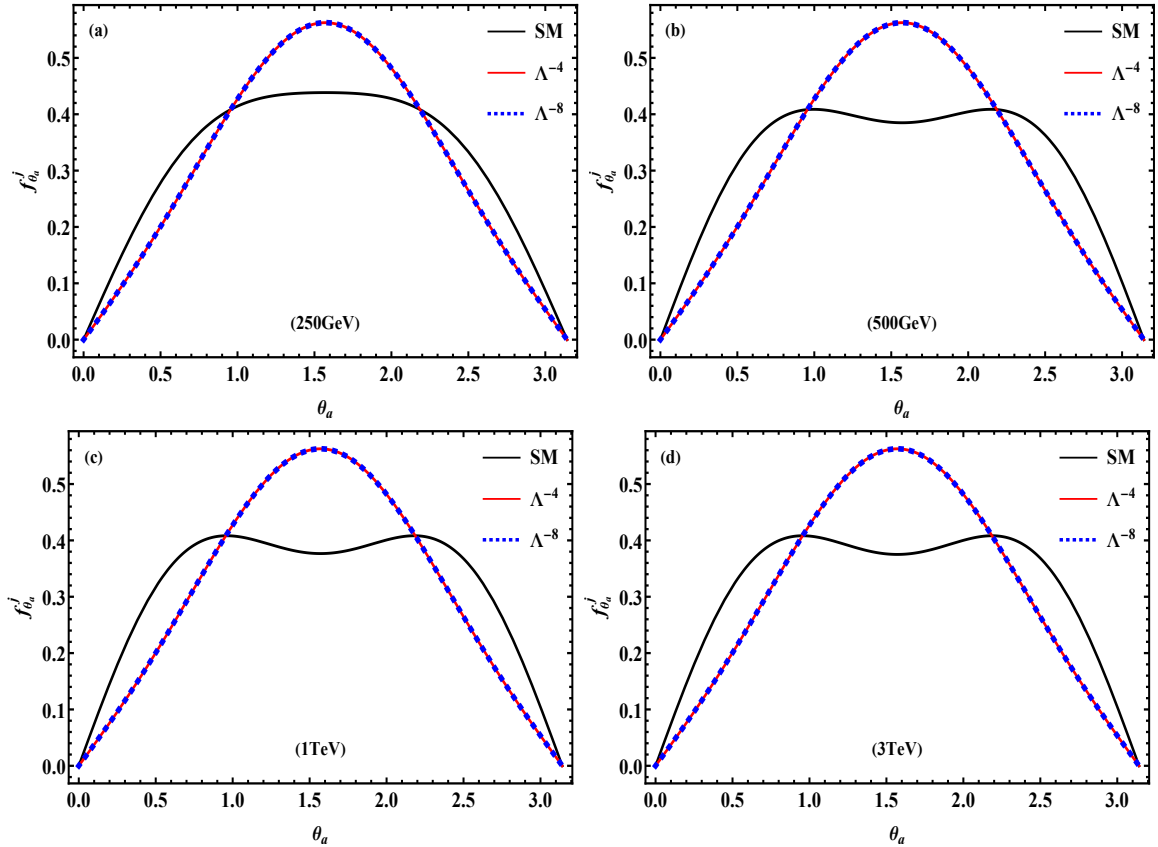


Figure 5: Normalized angular distribution in the polar angle  $\theta_a$  in the  $Z$  decay frame for different collider energies,  $\sqrt{s} = (0.25, 0.5, 1, 3)$  TeV, as shown in plots (a)-(d) respectively. In each plot, the black, red and blue curves denote the contributions from the SM, the  $O(\Lambda^{-4})$  interference, and the  $O(\Lambda^{-8})$  term respectively, where the red and blue curves exactly overlap.

to  $\theta_a$  and  $\phi_a$  are similar to the corresponding distributions for the  $Z\gamma$  final states given in [6][7]. The SM and pure dimension-8 distributions in  $\phi_a$  are rather flat, whereas the  $O(\Lambda^{-4})$  interference terms are dominated by cosine functions.

It is of interest to examine the high-energy behaviors of the angular distribution functions. In the case of the angular distribution respect to the scattering angle  $\theta$ , the distribution from the SM, namely  $f_{\theta}^0$ , increases rapidly with collision energy in the small  $\sin\theta$  region, whereas the distribution from the  $O(\Lambda^{-4})$  interference term,  $f_{\theta}^1$ , decreases with energy and the distribution from the pure  $O(\Lambda^{-8})$  dimension-8 term,  $f_{\theta}^2$ , is rather flat. For all the functions  $f_{\theta_a}^j$ , the coefficients of all trigonometric functions approach constants in the high-energy limit  $s \gg M_Z^2$ . This is why Fig. 5 shows that the distributions in  $\theta_a$  are not sensitive to the collision energy  $\sqrt{s}$ , as we vary the collision energy over the range  $\sqrt{s} = (0.25, 0.5, 1, 3)$  TeV in the four plots. In the high-energy limit  $s \gg M_Z^2$  we can derive the following angular distributions with respect to the angle  $\phi_a$ :

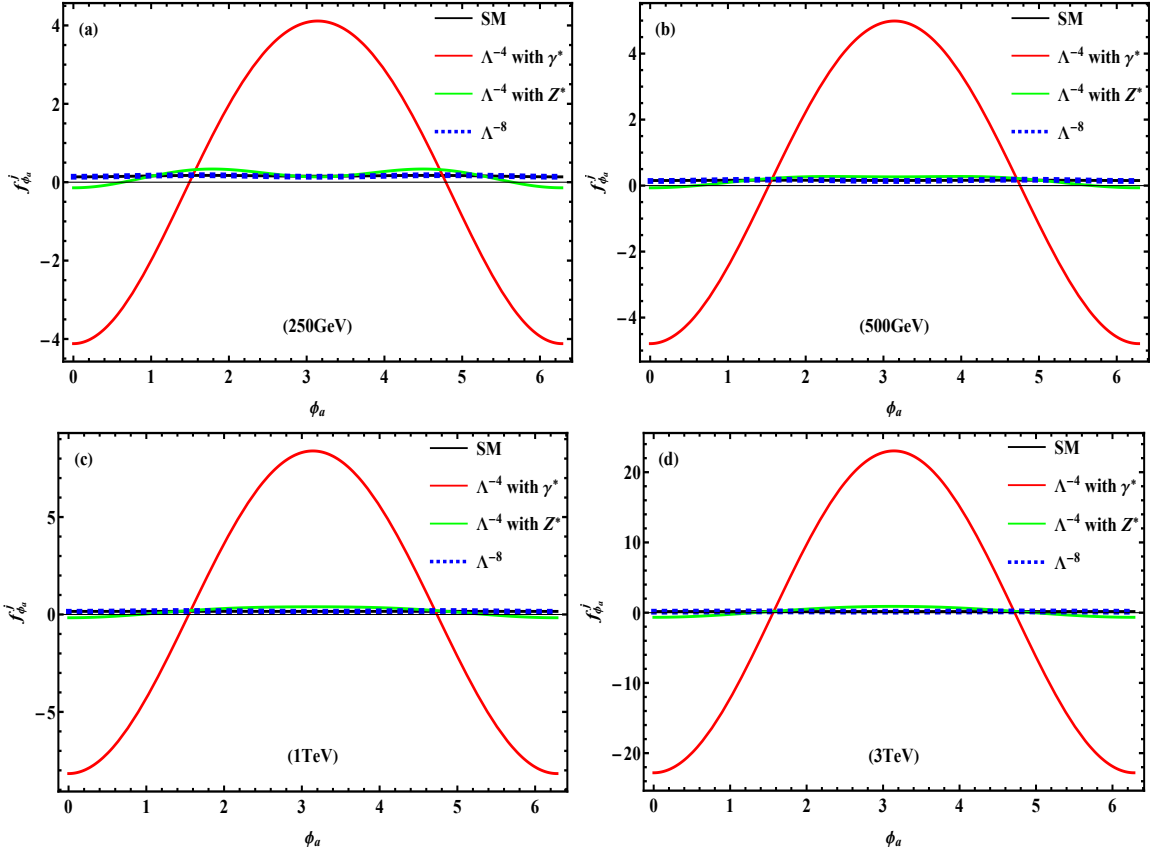


Figure 6: Normalized angular distributions in the azimuthal angle  $\phi_a$  of down-type quarks for different collider energies,  $\sqrt{s} = (0.25, 0.5, 1, 3)$  TeV, are shown in plots (a)-(d) respectively. In each plot, the black, red, and blue curves denote the contributions from the SM, the  $O(\Lambda^{-4})$  interference, and the pure dimension-8 term of  $O(\Lambda^{-8})$ , respectively, where the blue and black curves nearly overlap.

$$f_{\phi_a}^0 = \frac{1}{2\pi}, \quad (3.29a)$$

$$f_{\phi_a}^1 = \frac{1}{2\pi} - \frac{9\pi(c_L^V c_L^{Z^2} + c_R^V c_R^{Z^2})(f_L^2 - f_R^2)\sqrt{s} \cos\phi_a}{256(c_L^V c_L^{Z^2} - c_R^V c_R^{Z^2})(f_L^2 + f_R^2)M_Z} - \frac{\cos 2\phi_a}{8\pi}, \quad (3.29b)$$

$$f_{\phi_a}^2 = \frac{1}{2\pi} - \frac{\cos 2\phi_a}{16\pi}. \quad (3.29c)$$

From the above formulas, we see that the angular function  $f_{\phi_a}^0$  approaches the constant term  $\frac{1}{2\pi}$  for  $s \gg M_Z^2$ . We see in Eq.(3.28c) or Eq. (3.29c) that the value of the angular function  $f_{\phi_a}^2$  fluctuates around  $\frac{1}{2\pi}$  with a magnitude of only  $\frac{1}{16\pi}$ , which is why in Fig. 6 the angular functions  $f_{\phi_a}^0$  and  $f_{\phi_a}^2$  (shown as the black and blue curves) appear fairly flat and largely overlap with each other. In contrast, for the case of the angular function  $f_{\phi_a}^1$ , the coefficient of  $\cos\phi_a$  is enhanced by an energy factor  $\sqrt{s}/M_Z$ , and can be much larger than the constant term.

## 4 Probing $ZZV^*$ Couplings at $e^+e^-$ Colliders

In this Section we analyze systematically the capabilities of  $ZZ$  production in  $e^+e^-$  collisions followed by fermionic decays. We derive the nTGC signal sensitivity using the differential angular distributions

of the cross section with respect to all angles  $(\theta, \theta_a, \phi_a, \theta_b, \phi_b)$  for the case of  $Z$  bosons decaying to either leptons or quarks in Section 4.1. Then, in Section 4.2, we integrate over the angles  $\theta_b$  and  $\phi_b$ , which may be regarded as decay angles of  $Z$  bosons to neutrinos, thereby incorporating the neutrino decay channel of  $Z$  bosons. It is then shown in Sections 4.3 and 4.4 that the signal sensitivity may be significantly enhanced through the implementation of machine learning and the use of polarized  $e^\mp$  beams. Finally, in Section 4.5 we compare our results with those obtained in previous studies that considered the  $Z\gamma$  final state.

#### 4.1 Analyzing $ZZ$ Production via Leptonic/Hadronic Channels

For the present analysis, we define the observables:

$$\mathbb{O}_j \equiv \sigma_j \int_{\Omega} d\Omega |f_{\Omega}^j|, \quad (4.1)$$

where the angular distribution function

$$f_{\Omega}^j = \frac{d\sigma_j}{\sigma_j d\theta d\theta_a d\theta_b d\phi_a d\phi_b}, \quad (4.2)$$

and  $d\Omega = d\theta d\theta_a d\phi_a d\theta_b d\phi_b$ . We note that Eq.(4.1) integrates the absolute value of the angular distribution function  $f_{\Omega}^j$  over all the phase space. Though it is hard to obtain an analytic expression for Eq.(4.1), we can use the Monte-Carlo method to evaluate the integral (4.1) numerically.

Then, we calculate the signal significance:

$$\mathcal{Z}(f_a \bar{f}_a f_b \bar{f}_b) = \frac{|S_I|}{\Delta_{B_I}} = \frac{|\mathbb{O}_1(f_a \bar{f}_a f_b \bar{f}_b)|}{\sqrt{\sigma_0(f_a \bar{f}_a f_b \bar{f}_b)}} \times \sqrt{\mathcal{L} \times \epsilon}, \quad (4.3)$$

where  $\mathcal{L}$  is the integrated luminosity and  $\epsilon$  is the detection efficiency. When evaluating the signal significance using the above expression, we include only the final-state leptons and quarks, since neutrinos cannot be detected directly.

The differential angular distribution  $f_{\theta}^j$  with respect to the angle  $\theta$  is presented in Fig. 4, and we observe that SM background is concentrated predominantly within the forward and backward regions. Furthermore, as the scattering energy increases, the relative contributions of these SM backgrounds

$\sqrt{s}$ (TeV)	$\mathcal{L}$ (ab <sup>-1</sup> )	$ f_5^\gamma _{2\sigma}$	$ f_5^\gamma _{5\sigma}$	$ f_5^Z _{2\sigma}$	$ f_5^Z _{5\sigma}$
0.25	20	$2.1 \times 10^{-4}$	$5.2 \times 10^{-4}$	$2.6 \times 10^{-4}$	$6.4 \times 10^{-4}$
0.25	5	$4.1 \times 10^{-4}$	$1.0 \times 10^{-3}$	$5.1 \times 10^{-4}$	$1.3 \times 10^{-3}$
0.5	5	$4.0 \times 10^{-5}$	$1.0 \times 10^{-4}$	$8.6 \times 10^{-5}$	$2.2 \times 10^{-4}$
1	5	$8.3 \times 10^{-6}$	$2.1 \times 10^{-5}$	$2.2 \times 10^{-5}$	$5.4 \times 10^{-5}$
3	5	$8.9 \times 10^{-7}$	$2.2 \times 10^{-6}$	$2.6 \times 10^{-6}$	$6.5 \times 10^{-6}$
5	5	$3.2 \times 10^{-7}$	$7.9 \times 10^{-7}$	$9.2 \times 10^{-7}$	$2.3 \times 10^{-6}$

Table 3: Sensitivity reaches for the nTGC form factors  $f_5^\gamma$  and  $f_5^Z$  at the  $2\sigma$  and  $5\sigma$  levels, as derived by analyzing the reaction  $e^-e^+ \rightarrow f_a \bar{f}_a f_b \bar{f}_b$  (with  $f = \ell, q$ ), for a representative integrated luminosity  $\mathcal{L} = 5 \text{ ab}^{-1}$  at selected collision energies and an ideal detection efficiency  $\epsilon = 100\%$ .

within the forward and backward regions grows larger. Hence, imposing a constraint on the scattering angle  $\theta$  (such that a kinematic  $\sin \theta > \sin \delta$ ) serves to suppress the SM backgrounds, thereby enhancing the signal significance.

With the angular cut  $\delta = (0, 0.41, 0.34, 0.38, 0.37)$  for  $\sqrt{s} = (0.25, 0.5, 1, 3, 5)$  TeV, we derive the results in Table 3 for the sensitivities to the nTGC form factors ( $f_5^\gamma, f_5^Z$ ) and the results in Table 4 for the sensitivities to new physics cutoff scales  $\Lambda_j$  of the dimension-8 nTGC operators.

$\sqrt{s}$ (TeV)	$\mathcal{L}$ (ab $^{-1}$ )	$\Lambda_{\bar{B}W}^{2\sigma}$	$\Lambda_{\bar{B}W}^{5\sigma}$	$\Lambda_{3Z}^{2\sigma}$	$\Lambda_{3Z}^{5\sigma}$
0.25	20	1.3	1.0	1.0	.83
0.25	5	1.1	.87	.87	.69
0.5	5	2.0	1.6	1.4	1.1
1	5	2.9	2.3	1.9	1.5
3	5	5.1	4.0	3.3	2.6
5	5	6.6	5.2	4.2	3.4

Table 4: Sensitivity reaches for the new physics scales  $\Lambda_{\bar{B}W}$  and  $\Lambda_{3Z}$  (in TeV) via the reaction  $e^-e^+ \rightarrow f_a \bar{f}_a f_b \bar{f}_b$ , (with  $f = \ell, q$ ). The sensitivity reaches are shown at the  $2\sigma$  and  $5\sigma$  levels and for different collider energies. For illustration, we assume a representative integrated luminosity  $\mathcal{L} = 5 \text{ ab}^{-1}$  and an ideal detection efficiency  $\epsilon = 100\%$ .

Constraints on the new physics scale  $\Lambda_{\bar{B}W}$  are consistently stronger than those on  $\Lambda_{3Z}$ , and this advantage grows with increasing scattering energy. Limits on the new physics scale  $\Lambda$  generally strengthen as the scattering energy increases, primarily because the differences between the differential angular distributions of the interference signal  $f_\Omega^1$  and the SM background  $f_\Omega^0$  become more pronounced at higher scattering energies.

## 4.2 Analyzing the Invisible Decay Channel $Z \rightarrow \nu \bar{\nu}$

To compute the nTGC signal significance for the reaction  $e^-e^+ \rightarrow ZZ \rightarrow f \bar{f} \nu \bar{\nu}$  (with  $f = \ell, q$ ), we consider  $\theta_b$  and  $\phi_b$  to be the angles of the decay of one  $Z$  boson into neutrinos and integrate over them. Then, we compute the signal significance, with  $\theta_a$  and  $\phi_a$  being the angles of the other  $Z$  boson decays into leptons or quarks.

For this analysis, we define the following observable:

$$\mathbb{O}_j^n \equiv \sigma_j \int_{\Omega'} d\Omega' |f_{\Omega'}^j|, \quad (4.4)$$

where  $d\Omega' = d\theta d\theta_a d\phi_a$  and the partially integrated angular distribution function  $f_{\Omega'}^j$  is given by

$$f_{\Omega'}^j = \int f_\Omega^j d\theta_b d\phi_b. \quad (4.5)$$

With these, we compute the nTGC signal significance:

$$\mathcal{Z}_n(f_a \bar{f}_a) = \frac{|S_I|}{\Delta_{B_I}} = \frac{|\mathbb{O}_1^n(f_a \bar{f}_a)|}{\sqrt{\sigma_0(f_a \bar{f}_a)}} \times \sqrt{\mathcal{L} \times \epsilon}. \quad (4.6)$$

$\sqrt{s}$ (TeV)	$\mathcal{L}$ (ab $^{-1}$ )	$ f_5^\gamma _{f\bar{f}}$	$ f_5^\gamma _{\nu\bar{\nu}}$	$ f_5^\gamma _{\text{tot}}$
0.25	20	$(2.1, 5.2) \times 10^{-4}$	$(.57, 1.4) \times 10^{-3}$	$(1.9, 4.9) \times 10^{-4}$
0.25	5	$(.41, 1.0) \times 10^{-3}$	$(1.1, 2.8) \times 10^{-3}$	$(3.9, 9.7) \times 10^{-4}$
0.5	5	$(.40, 1.0) \times 10^{-4}$	$(1.0, 2.6) \times 10^{-4}$	$(3.8, 9.4) \times 10^{-5}$
1	5	$(.83, 2.1) \times 10^{-5}$	$(2.2, 5.4) \times 10^{-5}$	$(.78, 1.9) \times 10^{-5}$
3	5	$(.89, 2.2) \times 10^{-6}$	$(2.3, 5.7) \times 10^{-6}$	$(.83, 2.1) \times 10^{-6}$
5	5	$(3.2, 7.9) \times 10^{-7}$	$(.82, 2.0) \times 10^{-6}$	$(2.9, 7.4) \times 10^{-7}$

Table 5: Sensitivity reaches for the nTGC form factor  $f_5^\gamma$  at the  $(2\sigma, 5\sigma)$  level, as derived by analyzing the reactions  $e^-e^+ \rightarrow f_a \bar{f}_a f_b \bar{f}_b$ ,  $e^-e^+ \rightarrow f_a \bar{f}_a \nu \bar{\nu}$  (with  $f = \ell, q$ ) and their combination at selected collision energies, for a representative integrated luminosity  $\mathcal{L} = 5 \text{ ab}^{-1}$  and an ideal detection efficiency  $\epsilon = 100\%$ .

$\sqrt{s}$ (TeV)	$\mathcal{L}$ (ab $^{-1}$ )	$ f_5^Z _{f\bar{f}}$	$ f_5^Z _{\nu\bar{\nu}}$	$ f_5^Z _{\text{tot}}$
0.25	20	$(2.6, 6.4) \times 10^{-4}$	$(.52, 1.3) \times 10^{-3}$	$(2.3, 5.8) \times 10^{-4}$
0.25	5	$(.51, 1.3) \times 10^{-3}$	$(1.0, 2.6) \times 10^{-3}$	$(.46, 1.2) \times 10^{-3}$
0.5	5	$(.86, 2.2) \times 10^{-4}$	$(2.1, 5.3) \times 10^{-4}$	$(.80, 2.0) \times 10^{-4}$
1	5	$(2.2, 5.4) \times 10^{-5}$	$(.61, 1.5) \times 10^{-4}$	$(2.0, 5.1) \times 10^{-5}$
3	5	$(2.6, 6.5) \times 10^{-6}$	$(.78, 2.0) \times 10^{-5}$	$(2.5, 6.2) \times 10^{-6}$
5	5	$(.92, 2.3) \times 10^{-6}$	$(2.9, 7.3) \times 10^{-6}$	$(.88, 2.2) \times 10^{-6}$

Table 6: Sensitivity reaches for the nTGC form factor  $f_5^Z$  at the  $(2\sigma, 5\sigma)$  level, as derived by analyzing the reactions  $e^-e^+ \rightarrow f_a \bar{f}_a f_b \bar{f}_b$ ,  $e^-e^+ \rightarrow f_a \bar{f}_a \nu \bar{\nu}$  (with  $f = \ell, q$ ) and their combination at selected collision energies, for a representative integrated luminosity  $\mathcal{L} = 5 \text{ ab}^{-1}$  and an ideal detection efficiency  $\epsilon = 100\%$ .

We then derive the total signal significance for probing the nTGCs:

$$\mathcal{Z}_{\text{tot}} = \left[ \sum_{(a,b) \in (\ell,q)} \mathcal{Z}^2(f_a \bar{f}_a f_b \bar{f}_b) + \sum_{a \in (\ell,q)} \mathcal{Z}_n^2(f_a \bar{f}_a) \right]^{\frac{1}{2}}, \quad (4.7)$$

by using the angular cut  $\delta_n = (0, 0.27, 0.26, 0.34, 0.38)$  for  $\mathcal{Z}_n$  at each  $e^+e^-$  collider energy  $\sqrt{s} = (0.25, 0.5, 1, 3, 5) \text{ TeV}$ . We present our findings for the sensitivity reaches on the nTGC form factors  $(f_5^\gamma, f_5^Z)$  in Tables 5 and 6, and on the nTGC new physics scales in Table 7.

It can be seen that the limits on  $\Lambda^{\nu\bar{\nu}}$  are less stringent than those on  $\Lambda^{f\bar{f}}$ . This is due to the lower branching ratio of the  $Z$  boson decays to neutrinos as compared to its decays to charged fermions (including leptons and quarks):

$$\text{Br}[Z \rightarrow \nu\bar{\nu}] < \text{Br}[Z \rightarrow \ell\bar{\ell}, q\bar{q}], \quad (4.8)$$

and the absence of decay angle information. Consequently, incorporating the contribution from the neutrino decay channel of the  $Z$  boson yields only a modest improvement in the limit on the new physics scale  $\Lambda$ , as compared to the results obtained in Section 4.1 that include only  $Z$  boson decays to charged fermions.

$\sqrt{s}$ (TeV)	$\mathcal{L}$ (ab $^{-1}$ )	$\Lambda_{\bar{B}W}^{f\bar{f}}$	$\Lambda_{\bar{B}W}^{\nu\bar{\nu}}$	$\Lambda_{\bar{B}W}^{\text{tot}}$	$\Lambda_{3Z}^{f\bar{f}}$	$\Lambda_{3Z}^{\nu\bar{\nu}}$	$\Lambda_{3Z}^{\text{tot}}$
0.25	20	(1.3, 1.0)	(1.0, .80)	(1.3, 1.1)	(1.0, .83)	(.87, .69)	(1.1, .85)
0.25	5	(1.1, .87)	(.85, .68)	(1.1, .89)	(.87, .69)	(.73, .58)	(.90, .71)
0.5	5	(2.0, 1.6)	(1.5, 1.2)	(2.0, 1.6)	(1.4, 1.1)	(1.1, .87)	(1.4, 1.1)
1	5	(2.9, 2.3)	(2.3, 1.8)	(3.0, 2.4)	(1.9, 1.5)	(1.5, 1.2)	(2.0, 1.6)
3	5	(5.1, 4.0)	(4.0, 3.2)	(5.2, 4.1)	(3.3, 2.6)	(2.5, 2.0)	(3.3, 2.6)
5	5	(6.6, 5.2)	(5.2, 4.1)	(6.7, 5.3)	(4.2, 3.4)	(3.2, 2.5)	(4.3, 3.4)

Table 7: Sensitivity reaches for the new physics scales  $\Lambda_{\bar{B}W}$  and  $\Lambda_{3Z}$  (in TeV) through the reactions  $e^-e^+ \rightarrow f_a\bar{f}_a f_b\bar{f}_b$ ,  $e^-e^+ \rightarrow f_a\bar{f}_a\nu\bar{\nu}$  (with  $f = \ell, q$ ) and their combination. The bounds are shown at the  $(2\sigma, 5\sigma)$  level and for different  $e^+e^-$  collider energies. For illustration, we choose a representative integrated luminosity  $\mathcal{L} = 5 \text{ ab}^{-1}$  and an ideal detection efficiency  $\epsilon = 100\%$ .

### 4.3 Probability Cuts from Machine Learning

In this Section we explore the use of machine learning (ML) to improve the signal significance. ML has become a transformative tool in collider physics, addressing challenges in data analysis, pattern recognition, and theoretical modeling [23]. ML algorithms, such as boosted decision trees and deep neural networks, are widely used to distinguish rare particle collision signals from large background noise sources. These methods optimize event classification by learning complex correlations in high-dimensional datasets.

The core methodology is to use large samples of (labeled) simulated scattering events (explicitly tagged as belonging to the signal or background categories), which we use to train a classification algorithm to discover automatically optimal criteria for discriminating between the signal and backgrounds on the basis of measurements of physical quantities such as energies, momenta, angles, and their combinations within the events. After training, the classification algorithm functions as a classifier, which computes the probability that any experimental event belongs to the signal or background category.

We proceed by dividing phase space of the final states into a positive region  $R_+$  and a negative region  $R_-$  based on the signs of the angular distribution  $f_\Omega^1$  in Eq.(4.2) or  $f_{\Omega'}^1$  in Eq.(4.5),

$$R_+ : f_\Omega^1 > 0, \text{ or, } f_{\Omega'}^1 > 0, \quad (4.9a)$$

$$R_- : f_\Omega^1 < 0, \text{ or, } f_{\Omega'}^1 < 0. \quad (4.9b)$$

Subsequently, we categorize the signal  $S$  and background  $B$  into positive dataset  $(S_+, B_+)$  and negative dataset  $(S_-, B_-)$  according to  $R_+$  and  $R_-$ .

In this theoretical study, we generate events in `Mathematica` and then leverage its built-in ML function `Classify` with variables  $(\theta, \theta_a, \theta_b, \phi_a, \phi_b)$  to distinguish the nTGC signals from SM backgrounds. For the positive portion of the signal and background dataset  $(S_+$  and  $B_+)$ , we train a classifier  $C_{\text{sig-bkg}}^+$  capable of distinguishing between signals and backgrounds, and providing the probability that each event belongs to either category. We apply the same approach to the negative dataset

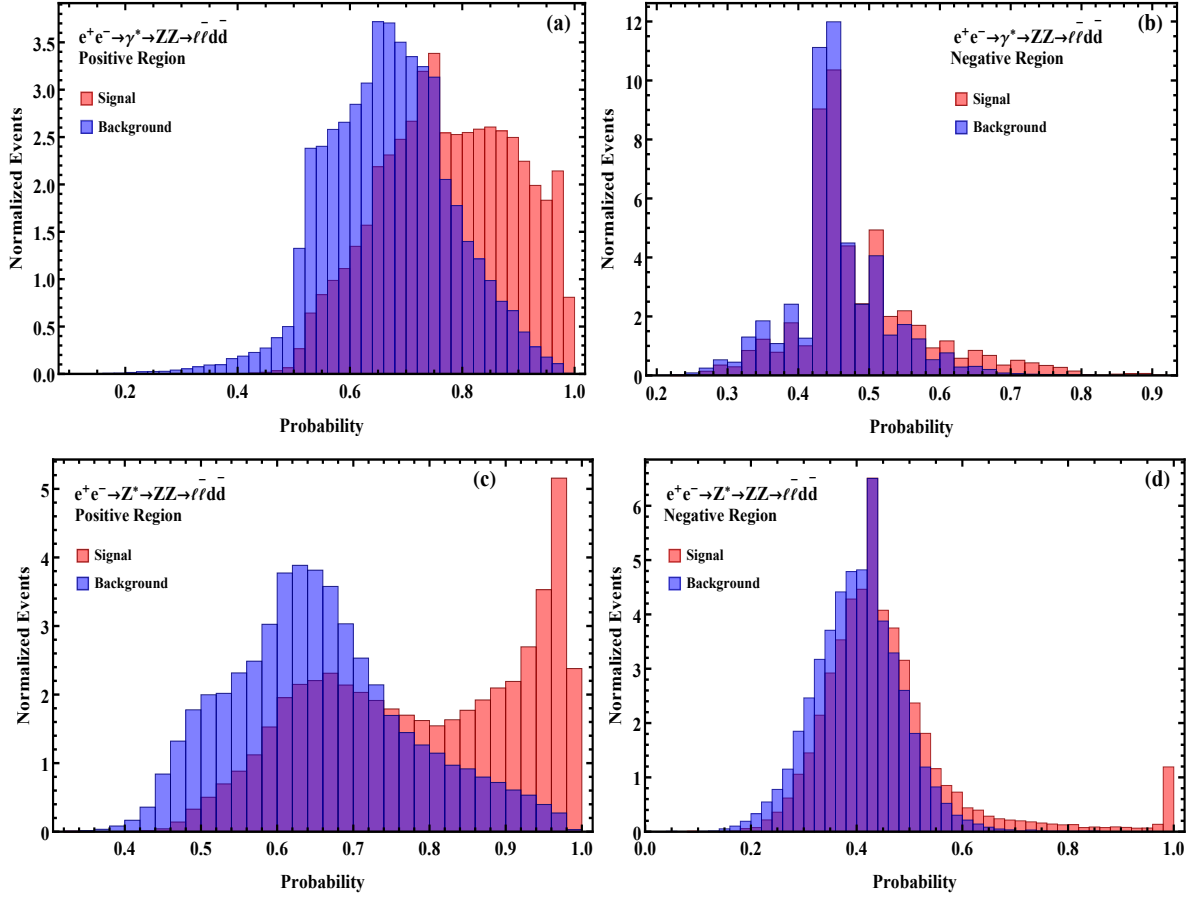


Figure 7: Probability distributions of events being signals and backgrounds respectively, for the case of  $e^+e^- \rightarrow V^* \rightarrow ZZ \rightarrow \ell\bar{\ell}d\bar{d}$  at a given collider energy  $\sqrt{s} = 250$  GeV. Here we choose the particular hadronic decay channel  $Z \rightarrow d\bar{d}$  (with  $d$  being down-type quarks) for illustration.

using a classifier  $C_{\text{sig-bkg}}^-$ . For instance, we illustrate in Fig. 7 the probability distributions for the collider energy  $\sqrt{s} = 250$  GeV. We choose the case of  $e^+e^- \rightarrow \gamma^* \rightarrow ZZ \rightarrow \ell\bar{\ell}d\bar{d}$  (with  $d$  being down-type quarks) in the positive region as a concrete example [as shown in Fig. 7(a)]. Then, we implement a probability cut  $P_{\gamma^*}^+(250\text{GeV}) \approx 0.75$  on the dataset to suppress the backgrounds and augment the signals. Similarly, the probability cuts ( $P_{\gamma^*}^-$ ,  $P_{Z^*}^+$ ,  $P_{Z^*}^-$ ) are obtained using classifier trained on the corresponding portion of the signal and background datasets.

Finally, we compute the total signal significance  $\mathcal{Z}_{\text{tot}}$  by using the significances from the positive region  $\mathcal{Z}_+$  and negative region  $\mathcal{Z}_-$ :

$$\mathcal{Z}_{\text{tot}} = \sqrt{\mathcal{Z}_+^2 + \mathcal{Z}_-^2}. \quad (4.10)$$

Employing this methodology, we have derived the sensitivity reaches on the nTGC form factors in Table 8 and on the nTGC new physics cutoff scales in Table 9.

We find that after applying machine learning to impose probabilistic constraints on the dataset and thereby suppressing the SM backgrounds, the phenomenological constraints on the new physics cutoff scale  $\Lambda$  are significantly enhanced as compared to the results prior to using machine learning. Specifically, in comparison with the results presented in Table 5 of Section 4.2, machine learning

$\sqrt{s}$ (TeV)	$\mathcal{L}$ (ab $^{-1}$ )	$ f_5^\gamma _{2\sigma}$	$ f_5^\gamma _{5\sigma}$	$ f_5^Z _{2\sigma}$	$ f_5^Z _{5\sigma}$
0.25	20	$7.6 \times 10^{-5}$	$1.9 \times 10^{-4}$	$1.1 \times 10^{-4}$	$2.8 \times 10^{-4}$
0.25	5	$1.5 \times 10^{-4}$	$3.8 \times 10^{-4}$	$2.3 \times 10^{-4}$	$5.7 \times 10^{-4}$
0.5	5	$1.6 \times 10^{-5}$	$4.1 \times 10^{-5}$	$4.0 \times 10^{-5}$	$1.0 \times 10^{-4}$
1	5	$3.7 \times 10^{-6}$	$9.4 \times 10^{-6}$	$9.2 \times 10^{-6}$	$2.3 \times 10^{-5}$
3	5	$3.6 \times 10^{-7}$	$9.0 \times 10^{-7}$	$9.1 \times 10^{-7}$	$2.3 \times 10^{-6}$
5	5	$9.4 \times 10^{-8}$	$2.3 \times 10^{-7}$	$2.2 \times 10^{-7}$	$5.6 \times 10^{-7}$

Table 8: Sensitivities to the nTGC form factors  $f_5^\gamma$  and  $f_5^Z$  at the  $2\sigma$  and  $5\sigma$  level after using ML probability cuts, as derived by analyzing the combination of  $e^-e^+ \rightarrow f_a \bar{f}_a f_b \bar{f}_b$  and  $e^-e^+ \rightarrow f_a \bar{f}_a \nu \bar{\nu}$  (with  $f = \ell, q$ ), with an ideal detection efficiency  $\epsilon = 100\%$ .

enhances the constraints on the form factor  $f_5^\gamma$  across different collider energies by 51% to 69%. The smallest enhancement of 51% is realized for  $|f_5^\gamma|_{5\sigma}$  at  $\sqrt{s} = 1$  TeV, whereas the largest enhancement of 69% occurs for  $|f_5^\gamma|_{5\sigma}$  at  $\sqrt{s} = 5$  TeV. Similarly, machine learning improves the constraints on the form factor  $f_5^Z$  by about (50–75)%. Here the smallest enhancement of 50% is found for  $|f_5^Z|_{2\sigma}$  at the collider energies  $\sqrt{s} = (0.25, 0.5)$  TeV, and for  $|f_5^Z|_{5\sigma}$  at the collider energy  $\sqrt{s} = 0.5$  TeV, which are both at the lower limit of the form factor range. Conversely, the strongest enhancement of 75% is achieved for  $|f_5^Z|_{2\sigma}$  at the collider energy  $\sqrt{s} = 5$  TeV.

Machine learning also improves the sensitivity reaches for the new physics scale  $\Lambda_{\tilde{B}W}$  across various collider energies by about (17–34)%. The smallest improvement of 17% is realized for  $\Lambda_{\tilde{B}W}^{\text{tot},5\sigma}$  at  $\sqrt{s} = 1$  TeV, whereas the largest improvement of 34% is achieved for  $\Lambda_{\tilde{B}W}^{\text{tot},5\sigma}$  at  $\sqrt{s} = 5$  TeV. Furthermore, machine learning improves the sensitivity reaches for  $\Lambda_{3Z}$  by about (14–42)% across different collider energies. Here the smallest improvement of 14% occurs for  $\Lambda_{3Z}^{\text{tot},2\sigma}$  at  $\sqrt{s} = 0.5$  TeV, and the largest improvement of 42% is found for  $\Lambda_{3Z}^{\text{tot},2\sigma}$  at  $\sqrt{s} = 5$  TeV. Interestingly, at lower collision energies (0.25 TeV and 0.5 TeV), the improvement facilitated by machine learning for  $\Lambda_{\tilde{B}W}$  is greater than that for  $\Lambda_{3Z}$ . Conversely, at higher collision energies of  $\sqrt{s} = (1-5)$  TeV, the improvement for the new physics scale  $\Lambda_{3Z}$  surpasses that for  $\Lambda_{\tilde{B}W}$ .

$\sqrt{s}$ (TeV)	$\mathcal{L}$ (ab $^{-1}$ )	$\Lambda_{\tilde{B}W}^{\text{tot},2\sigma}$	$\Lambda_{\tilde{B}W}^{\text{tot},5\sigma}$	$\Lambda_{3Z}^{\text{tot},2\sigma}$	$\Lambda_{3Z}^{\text{tot},5\sigma}$
0.25	20	1.7	1.3	1.3	1.0
0.25	5	1.4	1.1	1.1	.85
0.5	5	2.5	2.0	1.6	1.3
1	5	3.6	2.8	2.4	1.9
3	5	6.4	5.1	4.3	3.4
5	5	8.9	7.1	6.1	4.8

Table 9: Sensitivities ranges for the new physics scales  $\Lambda_{\tilde{B}W}$  and  $\Lambda_{3Z}$  (in TeV) via the combination of  $e^-e^+ \rightarrow f_a \bar{f}_a f_b \bar{f}_b$  and  $e^-e^+ \rightarrow f_a \bar{f}_a \nu \bar{\nu}$  (with  $f = \ell, q$ ) after using the ML probability cuts. The ranges are shown at the  $2\sigma$  and  $5\sigma$  level and for different energies. For illustration, we choose a representative integrated luminosity  $\mathcal{L} = 5 \text{ ab}^{-1}$  and an ideal detection efficiency  $\epsilon = 100\%$ .

## 4.4 Improvements from Polarized Electron and Positron Beams

In this subsection, we study the role of polarized  $e^-$  and  $e^+$  beams with  $(P_L^e, P_R^e) = (0.9, 0.65)$  denoting the fractions of (left, right)-handed (electrons, positrons) in the beam.<sup>3</sup> We present the sensitivity reaches on the nTGC form factors ( $f_5^\gamma, f_5^Z$ ) in Table 10 and on the nTGC new physics scales  $\Lambda_j$  in Tables 11.

$\sqrt{s}$ (TeV)	$\mathcal{L}$ ( $\text{ab}^{-1}$ )	$ f_5^\gamma _{2\sigma}$ (unpol, pol)	$ f_5^\gamma _{5\sigma}$ (unpol, pol)	$ f_5^Z _{2\sigma}$ (unpol, pol)	$ f_5^Z _{5\sigma}$ (unpol, pol)
0.25	20	$(7.6, 4.7) \times 10^{-5}$	$(1.9, 1.2) \times 10^{-4}$	$(1.1, .82) \times 10^{-4}$	$(2.8, 2.1) \times 10^{-4}$
0.25	5	$(1.5, .95) \times 10^{-4}$	$(3.8, 2.4) \times 10^{-4}$	$(2.3, 1.6) \times 10^{-4}$	$(5.7, 4.1) \times 10^{-4}$
0.5	5	$(1.6, 1.4) \times 10^{-5}$	$(4.1, 3.6) \times 10^{-5}$	$(4.0, 2.3) \times 10^{-5}$	$(1.0, .59) \times 10^{-4}$
1	5	$(3.7, 3.0) \times 10^{-6}$	$(9.4, 7.4) \times 10^{-6}$	$(9.2, 4.6) \times 10^{-6}$	$(2.3, 1.2) \times 10^{-5}$
3	5	$(3.6, 2.9) \times 10^{-7}$	$(9.0, 7.3) \times 10^{-7}$	$(9.1, 4.5) \times 10^{-7}$	$(2.3, 1.1) \times 10^{-6}$
5	5	$(9.4, 8.5) \times 10^{-8}$	$(2.3, 2.1) \times 10^{-7}$	$(2.2, 1.1) \times 10^{-7}$	$(5.6, 2.6) \times 10^{-7}$

Table 10: Sensitivity reaches for the nTGC form factors  $f_5^\gamma$  and  $f_5^Z$  at the  $2\sigma$  and  $5\sigma$  level, as derived by analyzing the combination of  $e^-e^+ \rightarrow f_a \bar{f}_a f_b \bar{f}_b$  and  $e^-e^+ \rightarrow f_a \bar{f}_a \nu \bar{\nu}$  (with  $f = \ell, q$ ), for (unpolarized, polarized)  $e^\mp$  beams in each entry, with the  $e^\mp$  beam polarizations  $(P_L^e, P_R^e) = (0.9, 0.65)$  for and an ideal detection efficiency  $\epsilon = 100\%$ .

$\sqrt{s}$ (TeV) (energy)	$\mathcal{L}$ ( $\text{ab}^{-1}$ )	$\Lambda_{\tilde{B}W}^{\text{tot}, 2\sigma}$ (unpol, pol)	$\Lambda_{\tilde{B}W}^{\text{tot}, 5\sigma}$ (unpol, pol)	$\Lambda_{3Z}^{\text{tot}, 2\sigma}$ (unpol, pol)	$\Lambda_{3Z}^{\text{tot}, 5\sigma}$ (unpol, pol)
0.25	20	(1.7, 1.9)	(1.3, 1.5)	(1.3, 1.4)	(1.0, 1.1)
0.25	5	(1.4, 1.6)	(1.1, 1.3)	(1.1, 1.2)	(.85, .92)
0.5	5	(2.5, 2.5)	(2.0, 2.0)	(1.6, 1.9)	(1.3, 1.5)
1	5	(3.6, 3.8)	(2.8, 3.0)	(2.4, 2.8)	(1.9, 2.3)
3	5	(6.4, 6.7)	(5.1, 5.4)	(4.3, 5.1)	(3.4, 4.0)
5	5	(8.9, 9.1)	(7.1, 7.3)	(6.1, 7.3)	(4.8, 5.8)

Table 11: Sensitivity reaches for the new physics cutoff scales  $\Lambda_{\tilde{B}W}$  and  $\Lambda_{3Z}$  (in TeV) through the combination of  $e^-e^+ \rightarrow f_a \bar{f}_a f_b \bar{f}_b$  and  $e^-e^+ \rightarrow f_a \bar{f}_a \nu \bar{\nu}$  (with  $f = \ell, q$ ), with (unpolarized, polarized)  $e^\mp$  beams in each entry. The bounds are presented at the  $2\sigma$  and  $5\sigma$  levels and for different collision energies. For illustration, we choose a representative integrated luminosity  $\mathcal{L} = 5 \text{ ab}^{-1}$ , an ideal detection efficiency  $\epsilon = 100\%$ , and the  $e^\mp$  beam polarizations  $(P_L^e, P_R^e) = (0.9, 0.65)$ .

Compared to the unpolarized results, polarized  $e^\mp$  beams enhance the sensitivity reaches on the form factor  $f_5^\gamma$  across various  $e^-e^+$  collider energies by (8.7–38)%. The smallest enhancement of 8.7% is realized for  $|f_5^\gamma|_{5\sigma}$  at  $\sqrt{s} = 5 \text{ TeV}$ , whereas the largest enhancement of 38% is achieved for  $|f_5^\gamma|_{2\sigma}$  at  $\sqrt{s} = 0.25 \text{ TeV}$  (with  $\mathcal{L} = 20 \text{ ab}^{-1}$ ). Moreover, polarized  $e^\mp$  beams improve the sensitivity bounds on the form factor  $f_5^Z$  by about (25–54)% across different collider energies. Here the smallest

<sup>3</sup>The degree of longitudinal beam polarization for electron  $e^-$  or positron  $e^+$  is defined as  $\hat{P} = P_R - P_L$  [24]. Because the sum of left-handed and right-handed fractions equals one ( $P_L + P_R = 1$ ), the left-handed and right-handed fractions of  $e^-$  and  $e^+$  can be derived as follows,  $P_{L,R}^e = \frac{1}{2}(1 \mp \hat{P}^e)$  and  $P_{L,R}^{\bar{e}} = \frac{1}{2}(1 \mp \hat{P}^{\bar{e}})$ . For example, an unpolarized beam of  $e^-$  or  $e^+$  has a vanishing degree of polarization  $\hat{P} = 0$ , whereas a polarized  $e^-$  beam with a fraction  $P_L^e = 90\%$  has  $\hat{P}^e = -0.8$  and a polarized  $e^+$  beam with a fraction  $P_R^e = 0.65\%$  has  $\hat{P}^e = 0.3$ .

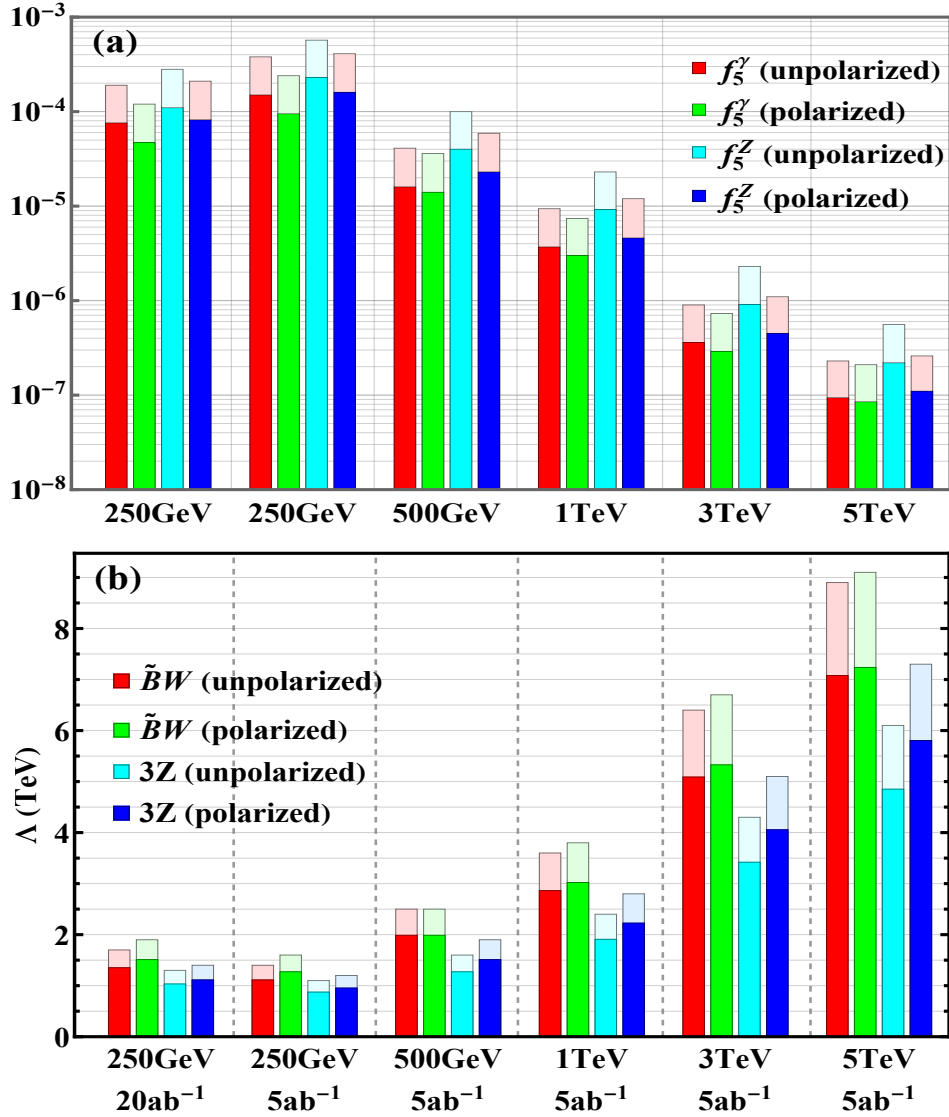


Figure 8: Sensitivity reaches for the nTGC form factors in plot (a) and for the nTGC new physics scales in plot (b) for various  $e^-e^+$  collision energies and integrated luminosities. In this figure, plot (a) presents the ( $2\sigma$ ,  $5\sigma$ ) sensitivity reaches in (heavy, light) colors, whereas plot (b) shows the ( $2\sigma$ ,  $5\sigma$ ) sensitivity reaches in (light, heavy) colors.

enhancement of 25% is found for  $|f_5^Z|_{5\sigma}$  at the collision energy  $\sqrt{s} = 0.25$  TeV (with  $20 \text{ ab}^{-1}$ ), and the largest enhancement of 54% occurs for  $|f_5^Z|_{5\sigma}$  at the collision energy  $\sqrt{s} = 5$  TeV.

We find that in most scenarios the beam polarizations can enhance  $\Lambda_{\tilde{B}W}$  by about 0.2 TeV as compared to the unpolarized case. However, the improvement of the sensitivity reaches for the new physics scale  $\Lambda_{3Z}$  facilitated by the polarized  $e^\mp$  beams is significantly more pronounced. Specifically, relative to the unpolarized results, the polarized  $e^\mp$  beams can improve the sensitivity reaches for  $\Lambda_{3Z}$  across different collision energies by about (7.7 – 21)%. The smallest improvement is 7.7% for  $\Lambda_{3Z}^{\text{tot}, 2\sigma}$  at the collision energy  $\sqrt{s} = 0.25$  TeV, whereas the largest improvement of 21% is achieved for  $\Lambda_{3Z}^{\text{tot}, 5\sigma}$  at the collision energy  $\sqrt{s} = 1$  TeV.

## 4.5 Analysis of Correlations between nTGC Parameters

In this subsection, we analyze the correlations between two nTGC form factors or two dimension-8 nTGC operators. We partition the phase space into  $2^5 = 32$  regions based on the signs of the cosine functions for the 5 angular variables  $(\theta, \theta_a, \theta_b, \phi_a, \phi_b)$ . Within each region, we compute the following observable:

$$\mathbb{O} = \sigma_1 \int d\Omega f_{\Omega}^1. \quad (4.11)$$

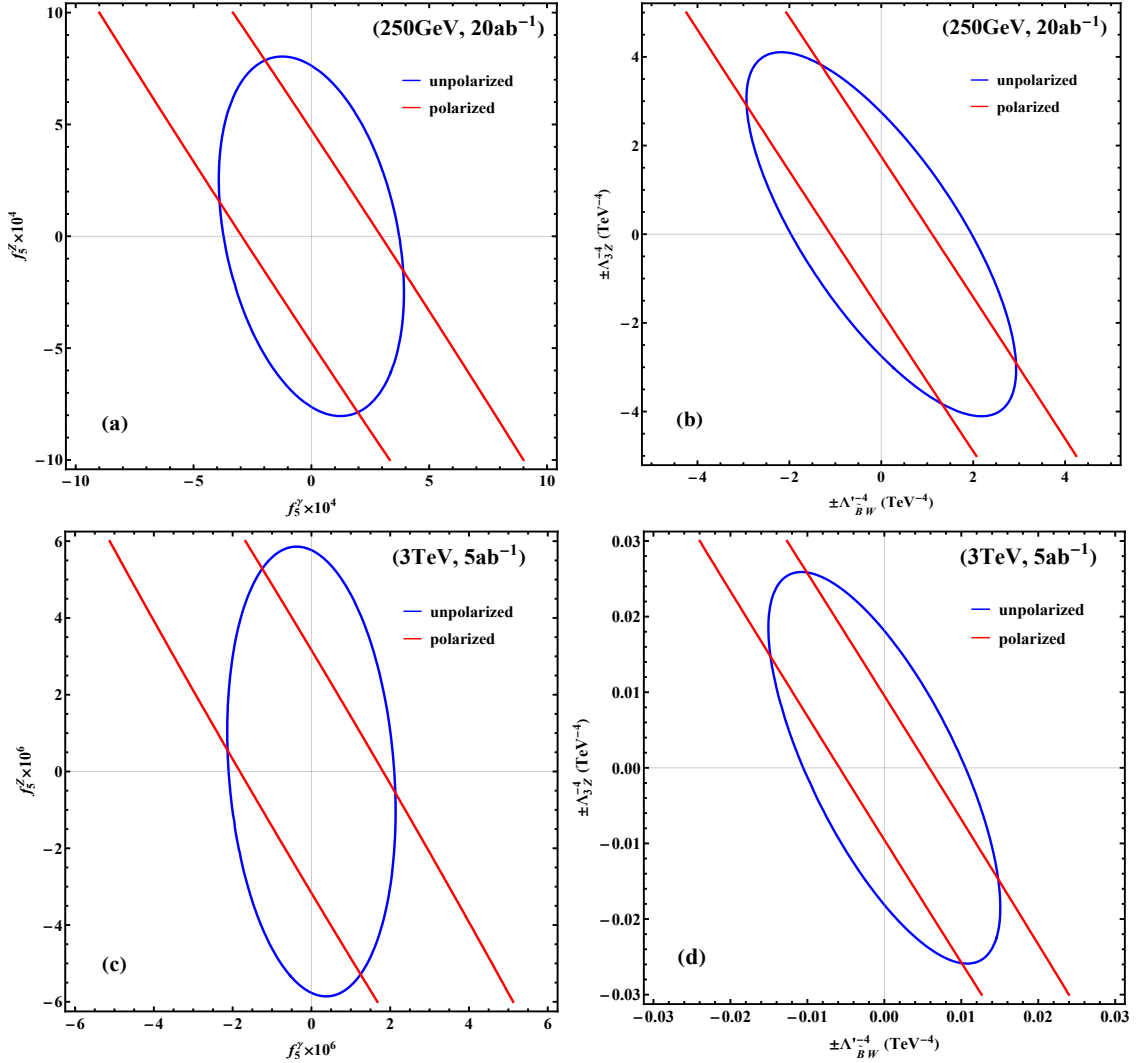


Figure 9: Sensitivity bounds on the nTGC form factors and on the nTGC new physics scales at  $2\sigma$  level, for the indicated collider energies and integrated luminosities. The plots (a)-(b) are shown for the collision energy  $\sqrt{s} = 250\text{GeV}$  and plots (c)-(d) are for the collision energy  $\sqrt{s} = 3\text{TeV}$ . The contours of the plots (a) and (c) depict the correlations between the form factors  $(f_5^\gamma, f_5^Z)$ , whereas the contours of the plots (b) and (d) present the correlations between the new physics scales  $(\Lambda'_{BW}, \Lambda'_{3Z})$ . In each plot, we compare results for the case of unpolarized  $e^\mp$  beams (blue curves) and the case of polarized  $e^\mp$  beams (red curves).

Then, we combine the contributions of two nTGC form factors or two dimension-8 nTGC operators

for Eq.(4.11) into a global  $\chi^2$  function:

$$\chi^2 = \sum_{i=1}^{32} \frac{\mathbb{O}_i^2}{\sigma_0^i} \times \mathcal{L} \times \epsilon, \quad (4.12)$$

where  $i$  sums over the 32 regions, and the observable  $\mathbb{O}_i$  incorporates contributions from the two form factors or two dimension-8 operators within the  $i$ -th region,  $\sigma_0^i$  denotes the SM background cross section in the  $i$ -th region. Minimizing the  $\chi^2$  function, we can derive correlated constraints on each pair of the nTGC form factors and of the nTGC cutoff scales. These constraints are presented in Fig. 9 as  $2\sigma$  contours, where the contours of the plots (a) and (c) depict the correlations between the form factors  $(f_5^\gamma, f_5^Z)$ , and the contours of the plots (b) and (d) present the correlations between the new physics scales  $(\Lambda'_{\tilde{B}W}, \Lambda_{3Z})$ . From this figure, we see that there are strong correlations in the polarized case. This is because, in terms of observable (4.11), the essential difference between these two dimension-8 operators lies in the distinct gauge couplings of the off-shell gauge boson ( $V=Z, \gamma$ ) to the incident electron-positron pair. The observable  $\mathbb{O}_i$  can be expressed as follows:

$$\mathbb{O}_i = (f_5^Z c_L^Z + f_5^\gamma c_L^\gamma) P_L^e P_R^{\bar{e}} A_i + (f_5^Z c_R^Z + f_5^\gamma c_R^\gamma) (1 - P_L^e) (1 - P_R^{\bar{e}}) B_i, \quad (4.13)$$

where the values of coefficients  $A_i$  and  $B_i$  depend on region  $i$ . In the polarized case  $(P_L^e, P_R^{\bar{e}}) = (0.9, 0.65)$ , the vast majority of incident electrons are left-handed, thus the right-handed component makes only a minor contribution to the above expression. Under these conditions, the distinction between the two dimension-8 operators reduces to just an overall factor, which explains why these operators exhibit strong correlation.

## 4.6 Comparison with Previous Results

In this subsection we compare our present sensitivity analysis for probing nTGCs via  $ZZ$  final states with those bounds extracted from our previous study [6][4] via the  $Z\gamma$  final state.

Using Table 3 of Ref. [6], we extract the sensitivity reaches for the nTGC new physics scale  $\Lambda_{\tilde{B}W}$  obtained via the  $Z\gamma$  channel and compare them with the present reaches for  $\Lambda_{\tilde{B}W}$  obtained via the  $ZZ$  channel, which are summarized in Table 12. In parallel, we can convert the sensitivity reaches for the nTGC new physics scale  $\Lambda_{\tilde{B}W}$  obtained via the  $Z\gamma$  channel in Ref. [6] to the corresponding reaches for the nTGC form factor  $h_3^Z$  obtained the via  $Z\gamma$  channel [4], which are then compared to the present reaches for the form factor  $f_5^\gamma$  obtained via the  $ZZ$  channel in Table 13.

It is evident that the sensitivity reaches for the nTGC new physics scales derived by the present study are significantly stronger than those reported in Ref. [6]. The current improvement is primarily attributable to the utilization of the fully differential angular distribution  $f_\Omega^1$  incorporating all angular variables  $(\theta, \theta_a, \phi_a, \theta_b, \phi_b)$ , combined with machine learning classification algorithms that efficiently discriminate the nTGC signal from SM backgrounds. Specifically, the sensitivity reaches for the new physics scale  $\Lambda_{\tilde{B}W}$  established by the present study exhibit an enhancement of (13.4–57.8)% as compared to the previous bounds of Ref. [6]. The smallest improvement of 13.4% occurs for  $\Lambda_{\tilde{B}W}^{\text{tot}, 5\sigma}$  in

the unpolarized case at the collider energy  $\sqrt{s} = 0.25$  TeV, whereas the largest improvement of 57.8% is achieved for  $\Lambda_{\tilde{B}W}^{\text{tot},5\sigma}$  in the unpolarized case at the collider energy  $\sqrt{s} = 5$  TeV.

Energy/Bounds	Previous Results [6]		Present Results	
$\sqrt{s}$ (TeV) (collider energy)	$\Lambda_{\tilde{B}W}^{\text{tot},2\sigma}$ (unpol, pol)	$\Lambda_{\tilde{B}W}^{\text{tot},5\sigma}$ (unpol, pol)	$\Lambda_{\tilde{B}W}^{\text{tot},2\sigma}$ (unpol, pol)	$\Lambda_{\tilde{B}W}^{\text{tot},5\sigma}$ (unpol, pol)
0.25	(1.2, 1.3)	(.97, 1.0)	(1.4, 1.6)	(1.1, 1.3)
0.5	(1.8, 1.9)	(1.4, 1.4)	(2.5, 2.5)	(2.0, 2.0)
1	(2.6, 2.6)	(2.0, 2.1)	(3.6, 3.8)	(2.8, 3.0)
3	(4.3, 4.5)	(3.5, 3.6)	(6.4, 6.7)	(5.1, 5.4)
5	(5.7, 5.9)	(4.5, 4.7)	(8.9, 9.1)	(7.1, 7.3)

Table 12: Comparison of our previous sensitivity reaches for the nTGC new physics scale  $\Lambda_{\tilde{B}W}$  obtained via the  $Z\gamma$  channel [6] with the present sensitivity reaches obtained via the  $ZZ$  channel, shown in TeV units. The previous reaches were derived for the  $Z\gamma$  channel with  $Z \rightarrow q\bar{q}$  [6] (shown in the 2nd and 3rd columns), whereas the present reaches are derived for the  $ZZ$  channel with  $Z \rightarrow q\bar{q}, \ell\bar{\ell}, \nu\bar{\nu}$  (shown in the 4th and 5th columns). These reaches are presented at  $2\sigma$  and  $5\sigma$  levels and for different collider energies. In each entry the bounds correspond to (unpolarized, polarized)  $e^\mp$  beams, with beam polarizations  $(P_L^e, P_R^e) = (0.9, 0.65)$ . For illustration, we choose a representative integrated luminosity  $\mathcal{L} = 5 \text{ ab}^{-1}$  and an ideal detection efficiency  $\epsilon = 100\%$ .

The present sensitivity reaches for the nTGC form factors also surpass the previous reaches found in Ref. [4]. For instance, we find that the sensitivity reaches for the nTGC form factors exhibit enhancements of about (44.1–84.7)% as compared to the reaches found in [4]. The minimal improvement of 44.1% is realized for the unpolarized limit of  $|f_5^\gamma|_{5\sigma}$  at the collider energy  $\sqrt{s} = 0.25$  TeV, whereas the most significant enhancement of 84.7% is achieved for  $|f_5^\gamma|_{5\sigma}$  in the unpolarized case at the collider energy  $\sqrt{s} = 5$  TeV.

Energy/Bounds	Previous Results [4]		Present Results	
$\sqrt{s}$ (TeV) (collider energy)	$ h_3^Z _{2\sigma}$ (unpol, pol)	$ h_3^Z _{5\sigma}$ (unpol, pol)	$ f_5^\gamma _{2\sigma}$ (unpol, pol)	$ f_5^\gamma _{5\sigma}$ (unpol, pol)
0.25	$(2.7, 2.3) \times 10^{-4}$	$(6.8, 6.0) \times 10^{-4}$	$(1.5, .95) \times 10^{-4}$	$(3.8, 2.4) \times 10^{-4}$
0.5	$(6.2, 5.2) \times 10^{-5}$	$(1.6, 1.4) \times 10^{-4}$	$(1.6, 1.4) \times 10^{-5}$	$(4.1, 3.6) \times 10^{-5}$
1	$(1.5, 1.2) \times 10^{-5}$	$(3.8, 3.1) \times 10^{-5}$	$(3.7, 3.0) \times 10^{-6}$	$(9.4, 7.4) \times 10^{-6}$
3	$(1.7, 1.4) \times 10^{-6}$	$(4.0, 3.6) \times 10^{-6}$	$(3.6, 2.9) \times 10^{-7}$	$(9.0, 7.3) \times 10^{-7}$
5	$(5.8, 4.9) \times 10^{-7}$	$(1.5, 1.3) \times 10^{-6}$	$(9.4, 8.5) \times 10^{-8}$	$(2.3, 2.1) \times 10^{-7}$

Table 13: Comparison of our previous sensitivity reaches for the nTGC form factors obtained via the  $Z\gamma$  channel [4] with the present sensitivity reaches obtained via the  $ZZ$  channel. The previous reaches were derived for the  $Z\gamma$  channel with  $Z \rightarrow q\bar{q}$  (shown in the 2nd and 3rd columns), whereas the present bounds are derived for the  $ZZ$  channel with  $Z \rightarrow q\bar{q}, \ell\bar{\ell}, \nu\bar{\nu}$  (shown in the 4th and 5th columns). These reaches are presented at  $2\sigma$  and  $5\sigma$  levels and for different collider energies respectively. In each entry the reaches correspond to (unpolarized, polarized)  $e^\mp$  beams, with beam polarizations  $(P_L^e, P_R^e) = (0.9, 0.65)$ . For illustration, we choose a representative integrated luminosity  $\mathcal{L} = 5 \text{ ab}^{-1}$  and an ideal detection efficiency  $\epsilon = 100\%$ .

## 5 Conclusions

Neutral triple gauge couplings (nTGCs) do not exist within the Standard Model (SM), nor do they receive contributions from any dimension-6 SMEFT operators. Hence, the nTGCs provide an important window for probing new physics beyond the SM that can be used to probe directly new physics encoded by dimension-8 SMEFT operators. The previous phenomenological studies [2]-[11] and experimental measurements [15][16] mainly focused on the  $Z\gamma V^*$  nTGCs (with  $V = Z, \gamma$ ) and did not probe the triple  $Z$  boson coupling  $ZZZ^*$ .

In this work, we formulated the nTGC form factors of  $ZZV^*$  ( $V = Z, \gamma$ ) that are compatible with the spontaneous breaking of the  $SU(2)\otimes U(1)$  electroweak gauge symmetry and consistently match the dimension-8 nTGC operators in the broken phase. We have systematically studied the sensitivities of probing both the  $ZZV^*$  form factors and new physics scales through the reaction process  $e^-e^+ \rightarrow ZZ \rightarrow f_a \bar{f}_a f_b \bar{f}_b$  (with  $f_a = \ell, q$  and  $f_b = \ell, q, \nu$ ) at high energy  $e^+e^-$  colliders, including CEPC, FCC-ee, ILC and CLIC. We have analyzed the signal significance and derived sensitivity reaches for probing the nTGC form factors  $f_5^V$  and the corresponding nTGC new physics scales  $\Lambda_j$ , which were summarized in Figs. 8(a) and 8(b).

In Section 2 we studied how the nTGC couplings of  $ZZV^*$  can arise from the relevant dimension-8 SMEFT operators as shown in Eq.(2.4) and Table 1. In particular, we constructed the dimension-8 nTGC operator  $\mathcal{O}_{3Z}$  in Eq.(2.6) that contributes to the  $ZZZ^*$  vertex only, but not to the  $ZZ\gamma^*$  vertex, as shown in Table 1 and Eq.(2.8). This is in contrast with the other operator  $\mathcal{O}_{\tilde{B}W}$  that contributes to the  $ZZ\gamma^*$  vertex alone, as shown in Table 1 and Eq.(2.9). We presented the consistent formulation of the nTGC form factors that are compatible with the full SM gauge symmetry  $SU(2)\otimes U(1)$  with spontaneous electroweak symmetry breaking. The unitarity constraints on the nTGCs were derived in Table 2 of Section 2.2 and are much weaker than the sensitivity bounds derived for the collider probes in Section 4.

In Section 3, we derived the scattering amplitudes, cross sections, and angular distributions for the reaction process  $e^-e^+ \rightarrow ZZ$ . We analyzed systematically the contributions from both the SM and nTGCs, as given analytically in Eqs.(3.23), (3.27) and (3.28). With these we demonstrated the differences in their differential angular distributions, as shown in Figs. 4–6. These are important for our phenomenological analysis of probing the nTGCs in the following Section 4.

In Section 4, we presented a systematic analysis of the  $ZZ$  production in different fermionic decay channels at various  $e^+e^-$  colliders. We computed the signal significance using the differential angular distributions of the cross section, considering both the visible leptonic and hadronic decay channels and the invisible decay channel ( $Z \rightarrow \nu\bar{\nu}$ ). The estimated sensitivity reaches for probing the nTGC form factors are shown in Tables 3,5,6 and for probing the nTGC new physics scales are shown in Tables 4,7. These sensitivity limits are presented for the leptonic and hadronic  $Z$ -decay channels in Sections 4.1 and for the invisible  $Z$ -decay channels in Section 4.2. We studied the significant improvements of the sensitivity reaches achieved through the use of machine learning in Section 4.3. We further derived the

enhanced sensitivity bounds on probing the nTGCs by using the polarized  $e^\pm$  beams in Section 4.4. Our optimal sensitivity bounds were summarized in Fig. 8, whereas the correlations between the nTGC form factors and between the nTGC new physics scales were presented in Figs. 9(a)(c) and Figs. 9(b)(d) respectively. Finally, Section 4.6 compared the sensitivity reaches on probing the nTGCs as obtained in this work with previous studies [4][6]. We have demonstrated that the sensitivity bounds on probing the nTGC form factors and the nTGC new physics scales as given in this work are significantly stronger, primarily due to the use of fully differential angular distributions combined with machine learning technique.

## Acknowledgements

The work of J.E. was supported in part by the United Kingdom STFC Grant ST/T000759/1. The works of HJH, RQX and SPZ were supported in part by the National Natural Science Foundation of China (NSFC) under Grants 12175136 and 12435005, by the State Key Laboratory of Dark Matter Physics, by the Key Laboratory for Particle Astrophysics and Cosmology (MOE), and by the Shanghai Key Laboratory for Particle Physics and Cosmology. RQX was also supported in part by the NSFC under Grants 12175006, 12188102 and 12061141002, by the Ministry of Science and Technology of China under Grant 2023YFA1605800, and by the state key laboratory of nuclear physics and technology.

## References

- [1] For recent reviews, John Ellis, [arXiv:2105.14942 [hep-ph]], in the conference proceedings of “Beyond Standard Model: From Theory to Experiment” (BSM-2021), Zewail City, Egypt, March 29-31, 2021; I. Brivio and M. Trott, Phys. Rept. 793 (2019) 1 [arXiv:1706.08945 [hep-ph]]; and references therein.
- [2] J. Ellis, H.-J. He, and R.-Q. Xiao, Science China (2025) [arXiv:2504.13135 [hep-ph]].
- [3] J. Ellis, H.-J. He, and R.-Q. Xiao, Phys. Rev. D 108 (2023) L111704, no.11 [arXiv:2308.16887 [hep-ph]].
- [4] J. Ellis, H. J. He, R.-Q. Xiao, Phys. Rev. D 107 (2023) 035005, no.3 [arXiv:2206.11676 [hep-ph]].
- [5] D. Liu, R.-Q. Xiao, S. Li, J. Ellis, H.-J. He, and R. Yuan, Front. Phys. 20 (2025) 015201, no.1 [arXiv:2404.15937 [hep-ph]].
- [6] J. Ellis, H.-J. He, R.-Q. Xiao, Science China (Phys. Mech. Astron.) 64 (2021) 221062, no.2, [arXiv:2008.04298 [hep-ph]].
- [7] J. Ellis, S. F. Ge, H.-J. He, R.-Q. Xiao, Chin. Phys. C 44 (2020) 063106, no.6, [arXiv:1902.06631 [hep-ph]].

- [8] J. Ellis, H.-J. He, R.-Q. Xiao, S.-P. Zeng, and J. Zheng, Phys. Rev. D 111 (2025) 015007, no.1, [arXiv:2408.12508 [hep-ph]].
- [9] See also, R. Cepedello, F. Esser, M. Hirsch, and V. Sanz, JHEP 07 (2024) 275, [JHEP 12 (2024) 084 (erratum)], [arXiv:2402.04306 [hep-ph]].
- [10] G. J. Gounaris, J. Layssac, and F. M. Renard, Phys. Rev. D 61 (2000) 073013 [arXiv:hep-ph/9910395 [hep-ph]]; Phys. Rev. D 62 (2000) 073013 [arXiv:hep-ph/0003143 [hep-ph]].
- [11] C. Degrande, JHEP 1402 (2014) 101 [arXiv:1308.6323 [hep-ph]].
- [12] W. Buchmuller and D. Wyler, Nucl. Phys. B 268 (1986) 621; B. Grzadkowski, M. Iskrzynski, M. Misiak, and J. Rosiek, JHEP 10 (2010) 085 [arXiv:1008.4884 [hep-ph]]; and references therein.
- [13] E.g., J. Ellis, V. Sanz, and T. You, JHEP 1407 (2014) 036 [arXiv:1404.3667 [hep-ph]] and JHEP 1503 (2015) 157 [arXiv:1410.7703 [hep-ph]]; H. J. He, J. Ren, and W. Yao, Phys. Rev. D 93 (2016) 015003 [arXiv:1506.03302 [hep-ph]]; J. Ellis and T. You, JHEP 03 (2016) 089 [arXiv:1510.04561 [hep-ph]]; S. F. Ge, H. J. He, and R. Q. Xiao, JHEP 10 (2016) 007 [arXiv:1603.03385 [hep-ph]]; J. de Blas et al., JHEP 12 (2016) 135 [arXiv:1608.01509 [hep-ph]]; F. Ferreira, B. Fuks, V. Sanz, and D. Sengupta, Eur. Phys. J. C 77 (2017) 675 [arXiv:1612.01808 [hep-ph]]; J. Ellis, P. Roloff, V. Sanz, and T. You, JHEP 05 (2017) 096 [arXiv:1701.04804 [hep-ph]]; G. Durieux, C. Grojean, J. Gu and K. Wang, JHEP 09 (2017) 014 [arXiv:1704.02333 [hep-ph]]; T. Barklow et al., Phys. Rev. D 97 (2018) 053003 [arXiv:1708.08912 [hep-ph]]; C. W. Murphy, Phys. Rev. D 97 (2018) 015007 [arXiv:1710.02008 [hep-ph]]; J. Ellis, C. W. Murphy, V. Sanz, and T. You, JHEP 06 (2018) 146 [arXiv:1803.03252 [hep-ph]]; G. N. Remmen and N. L. Rodd, JHEP 12 (2019) 032 [arXiv:1908.09845 [hep-ph]]; A. Gutierrez-Rodriguez, M. Koksal, A. A. Billur, M. A. Hernandez-Ruiz, J. Phys. G 47 (2020) 055005 [arXiv:1910.02307 [hep-ph]]; M. Koksal, A. A. Billur, A. Gutierrez-Rodriguez, and M. A. Hernandez-Ruiz, Phys. Lett. B 808 (2020) 135661 [arXiv:1910.06747 [hep-ph]]; J. Ellis, M. Madigan, K. Mimasu, V. Sanz, and T. You, JHEP 04 (2021) 279 [arXiv:2012.02779 [hep-ph]]. and references therein.
- [14] V. Khachatryan *et al.*, [CMS Collaboration], “Measurement of the  $Z\gamma \rightarrow \nu\bar{\nu}\gamma$  production cross section in  $pp$  collisions at  $\sqrt{s} = 8\text{TeV}$  and limits on anomalous  $ZZ\gamma$  and  $Z\gamma\gamma$  trilinear gauge boson couplings”, Phys. Lett. B 760 (2016) 448-468 [arXiv: 1602.07152 [hep-ex]].
- [15] M. Aaboud *et al.*, [ATLAS Collaboration], “Measurement of the  $Z \rightarrow \nu\bar{\nu}$  production cross section in  $pp$  collisions at  $\sqrt{s} = 13\text{TeV}$  with the ATLAS detector and limits on anomalous triple gauge-boson couplings”, JHEP 12 (2018) 010 [arXiv:1810.04995 [hep-ex]].
- [16] ATLAS Collaboration, “*Measurements of  $Z\gamma$  differential cross sections and search for neutral triple gauge couplings in  $pp$  collisions at  $\sqrt{s} = 13\text{TeV}$  with the ATLAS detector*”, ATLAS-CONF-2025-001, April, 2025.

- [17] E.g., S. Jahedi, JHEP (2023) 31 [arXiv:2305.11266 [hep-ph]]; S. Spor, E. Gurkanli and M. Köksal, arXiv:2302.08245 [hep-ph]; S. Jahedi and J. Lahiri, JHEP 04 (2023) 085 [arXiv:2212.05121 [hep-ph]]; S. Spor, Nucl. Phys. B 991 (2023) 116198 [arXiv:2207.11585 [hep-ph]]; A. Senol, S. Spor, E. Gurkanli, V. Cetinkaya, H. Denizli, and M. Köksal, Eur. Phys. J. Plus 137 (2022) 1354, no.12 [arXiv:2205.02912 [hep-ph]]; Q. Fu, J. C. Yang, C. X. Yue, and Y. C. Guo, Nucl. Phys. B 972 (2021) 115543 [arXiv:2102.03623 [hep-ph]]. A. Biekötter, P. Gregg, F. Krauss, and M. Schönherr, Phys. Lett. B 817 (2021) 136311 [arXiv:2102.01115 [hep-ph]]; A. Senol, H. Denizli, A. Yilmaz, I. Turk Cakir, K. Y. Oyulmaz, O. Karadeniz, and O. Cakir, Nucl. Phys. B 935 (2018) 365 [arXiv:1805.03475 [hep-ph]]. R. Rahaman and R. K. Singh, Nucl. Phys. B 948 (2019) 114754 [arXiv:1810.11657 [hep-ph]]; Eur. Phys. J. C 77 (2017) 521, no.8 [arXiv:1703.06437 [hep-ph]]; Eur. Phys. J. C 76 (2016) 539, no.10, [arXiv:1604.06677 [hep-ph]].
- [18] Y. C. Guo, C. J. Pan, M. Q. Ruan and J. C. Yang, arXiv:2411.04804 [hep-ph].
- [19] D. A. Dicus and H.-J. He, Phys. Rev. D 71 (2005) 093009 [arXiv:hep-ph/0409131 [hep-ph]]; Phys. Rev. Lett. 94 (2005) 221802 [arXiv:hep-ph/0502178 [hep-ph]].
- [20] M. Jacob and G. C. Wick, Ann. Phys. (N.Y.) 7 (1959) 404, no.7.
- [21] For a comprehensive review, H. J. He, Y. P. Kuang and C. P. Yuan, [arXiv:hep-ph/9704276 [hep-ph]] and DESY-97-056, in the proceedings of the workshop on “Physics at the TeV Energy Scale”, vol.72, p.119, 1996. See also, H. J. He and W. B. Kilgore, Phys. Rev. D 55 (1997) 1515; H. J. He, Y. P. Kuang and C. P. Yuan, Phys. Rev. D 51 (1995) 6463; Phys. Rev. D 55 (1997) 3038; H. J. He, Y. P. Kuang and X. Li, Phys. Lett. B 329 (1994) 278; Phys. Rev. D 49 (1994) 4842; Phys. Rev. Lett. 69 (1992) 2619; and references therein.
- [22] F. Englert and R. Brout, Phys. Rev. Lett. 13 (1964) 321; P. W. Higgs, Phys. Rev. Lett. 13 (1964) 508; Phys. Lett. 12 (1964) 132; G. S. Guralnik, C. R. Hagen and T. Kibble, Phys. Rev. Lett. 13 (1964) 585; T. Kibble, Phys. Rev. 155 (1967) 1554.
- [23] T. Plehn, A. Butter, B. Dillon, T. Heimel, C. Krause and R. Winterhalder, [arXiv:2211.01421 [hep-ph]].
- [24] K. Fujii, C. Grojean, and M. E. Peskin *et al.*, [arXiv:1801.02840 [hep-ph]].